



Swansea University
Prifysgol Abertawe



Cronfa - Swansea University Open Access Repository

This is an author produced version of a paper published in:
New Journal of Physics

Cronfa URL for this paper:
<http://cronfa.swan.ac.uk/Record/cronfa36264>

Paper:

Muller, M. Micromotion-enabled improvement of quantum logic gates with trapped ions. *New Journal of Physics*

This item is brought to you by Swansea University. Any person downloading material is agreeing to abide by the terms of the repository licence. Copies of full text items may be used or reproduced in any format or medium, without prior permission for personal research or study, educational or non-commercial purposes only. The copyright for any work remains with the original author unless otherwise specified. The full-text must not be sold in any format or medium without the formal permission of the copyright holder.

Permission for multiple reproductions should be obtained from the original author.

Authors are personally responsible for adhering to copyright and publisher restrictions when uploading content to the repository.

<http://www.swansea.ac.uk/library/researchsupport/ris-support/>



PAPER • OPEN ACCESS

Micromotion-enabled improvement of quantum logic gates with trapped ions

To cite this article: Alejandro Bermudez *et al* 2017 *New J. Phys.* **19** 113038

View the [article online](#) for updates and enhancements.

Related content

- [Driven geometric phase gates with trapped ions](#)
A Lemmer, A Bermudez and M B Plenio
- [Quantum transport of energy in controlled synthetic quantum magnets](#)
Alejandro Bermudez and Tobias Schaetz
- [Dynamical decoupling sequences for multi-qubit dephasing suppression and long-time quantum memory](#)
Gerardo A Paz-Silva, Seung-Woo Lee, Todd J Green et al.



PAPER

Micromotion-enabled improvement of quantum logic gates with trapped ions

OPEN ACCESS

RECEIVED

23 May 2017

REVISED

9 August 2017

ACCEPTED FOR PUBLICATION

17 August 2017

PUBLISHED

24 November 2017

Original content from this work may be used under the terms of the [Creative Commons Attribution 3.0 licence](#).

Any further distribution of this work must maintain attribution to the author(s) and the title of the work, journal citation and DOI.

Alejandro Bermudez^{1,2}, Philipp Schindler³, Thomas Monz³, Rainer Blatt^{3,4} and Markus Müller¹¹ Department of Physics, College of Science, Swansea University, Singleton Park, Swansea SA2 8PP, United Kingdom² Instituto de Física Fundamental, IFF-CSIC, Madrid E-28006, Spain³ Institute for Experimental Physics, University of Innsbruck, A-6020 Innsbruck, Austria⁴ Institute for Quantum Optics and Quantum Information of the Austrian Academy of Sciences, A-6020 Innsbruck, AustriaE-mail: bermudez.carballo@gmail.com**Keywords:** trapped ions, entangling gates, micromotion

Abstract

The micromotion of ion crystals confined in Paul traps is usually considered an inconvenient nuisance, and is thus typically minimized in high-precision experiments such as high-fidelity quantum gates for quantum information processing (QIP). In this work, we introduce a particular scheme where this behavior can be reversed, making micromotion beneficial for QIP. We show that using laser-driven micromotion sidebands, it is possible to engineer state-dependent dipole forces with a reduced effect of off-resonant couplings to the carrier transition. This allows one, in a certain parameter regime, to devise entangling gate schemes based on geometric phase gates with both a higher speed and a lower error, which is attractive in light of current efforts towards fault-tolerant QIP. We discuss the prospects of reaching the parameters required to observe this micromotion-enabled improvement in experiments with current and future trap designs.

1. Introduction

The possibility of harnessing the distinctive behavior of quantum-mechanical systems to process information in new ways has raised the interest of researchers for more than three decades now. This has given rise to the multi-disciplinary field of quantum information processing (QIP) [1], which could, for instance, have an impact on current cryptographic protocols [2], or revolutionize our approach to solve long-standing problems in quantum many-body physics [3]. Motivated by such remarkable applications, QIP has now turned into a mature field where experimentalists are using different technologies [4] to face the challenge of building registers of ever-increasing sizes, while trying to preserve and manipulate their quantum features for ever-longer periods of time.

Among these so-called *quantum technologies*, crystals of trapped and laser-cooled atomic ions [5–7] have played a leading role in the progress of QIP. Pioneering proposals to build a quantum-information processor based on trapped ions [8], and successfully implemented in the laboratory [9], have opened an active avenue of research with the ultimate goal of building a large-scale trapped-ion quantum computer [10]. As emphasized early in the literature [11], success in such an enterprise would require (i) a careful assessment of the possible imperfections of the quantum processor, which lead to errors in the computation, and (ii) a thorough study of the unavoidable coupling to an external environment, which degrades the quantum coherence responsible for the advantages of QIP. The former yields errors that can accumulate quickly since the information is not stored in classical binary variables [11], whereas the latter yields an exponential decrease of quantum coherence with the size of the register [12].

Despite such a daunting perspective, the subsequent development of quantum error correction showed that these difficulties can be overcome if (i) one encodes the information redundantly in an enlarged quantum mechanical system instead of using a bare quantum register, and (ii) errors are detected and corrected during the storage and processing of encoded states [13]. Increasing levels of protection against noise can be achieved e.g. by concatenating elementary quantum error correcting codes, or by storing logical states in global,

topological properties of larger quantum many-body systems [14]. It has been shown that *fault-tolerant* QIP is possible provided that errors, either due to imperfections of gates or to environmental decoherence, occur below certain critical rates. The particular threshold values depend on the details of the implementation, the noise model, and the chosen encoding. For circuit noise models, a common estimate for concatenated codes is around 10^{-4} [15], whereas topological codes typically offer higher error thresholds up to about 10^{-2} [14]. Essentially, once below the threshold, quantum error correction allows for slowing down the occurrence of errors at the level of the logical qubits, such that longer computations can tolerate noise on the physical qubits at a much higher rate. Trapped ions have already demonstrated remarkable progress in experimental demonstrations of quantum error correction [16–18].

In order to meet such a threshold, one must optimize the hardware (i.e. quantum technology) and the software (i.e. schemes to manipulate the quantum information), which can be understood as a built-in *error suppression*. At the software level, one can mitigate decoherence by encoding the information in a section of the Hilbert space that is more robust to the typical environmental noise, as occurs for decoherence-free subspaces [19, 20], and for the so-called clock-state qubits [21]. Regarding imperfections of gates, pulsed [22, 23] and continuous [24, 25] dynamical decoupling have also been implemented in ion traps. Another possible source of error arises in certain quantum technologies that exploit additional auxiliary (quasi)particles to mediate an entangling gate between distant qubits, since quantum/classical fluctuations affecting these (quasi)particles can introduce errors in the computation. Such is the situation with trapped ions, where phonons serve as a quantum bus to generate entanglement, and thermal fluctuations lead to significant errors when the ion crystals are not laser cooled to the groundstate [8]. In this respect, the development of gate schemes that minimize such thermal sensitivity has been of paramount importance to the field. These schemes typically use a *state-dependent dipole force* in the resolved-sideband regime, which forces the ions along a closed trajectory in phase space depending on the state of the qubits, either in the σ^z [26, 27] or σ^ϕ [28, 29] eigenstate basis, where $\sigma^\phi = -\cos(\phi)\sigma^y - \sin(\phi)\sigma^x$. This effectively leads to state-dependent multi-qubit geometric phases that can be exploited to generate entanglement, which underlies the remarkably low errors that have been achieved in experiments so far [30–32], with infidelities reaching values below 10^{-3} .

An increase of gate speed yields another clear route for further error suppression, as the environmental decoherence affecting the qubits, or other external sources of noise affecting the phonon bus, would have a smaller impact during a shorter computation. Schemes for ultra-fast entangling gates based on concatenated resonant state-dependent kicks have been studied in detail [33], which abandon the resolved-sideband regime to avoid the associated limitations on the gate speed. These schemes give a clear advantage provided that high laser repetition rates [34], and small laser intensity fluctuations [35], can be achieved in the laboratory. Pulse splitting techniques have been implemented in order to increase the number of pulses incident on the ion [36], increasing thus the repetition rate towards a regime where ultra-fast gates are expected to have small errors [34]. To overcome the stringent conditions on the laser intensity stability [35], dynamical decoupling approaches may have to be applied in order to minimize the error of each resonant state-dependent kick [37].

In order to avoid these technical difficulties, but still get an increase on gate speed with respect to previous realizations [27, 29], schemes based on state-dependent σ^z -forces with an increased laser intensity have also been studied [38], which take into account the leading-order corrections as one abandons the resolved-sideband regime. In this case, such corrections correspond to a time-dependent ac-Stark shift, which is usually neglected in the resolved-sideband limit [27], but starts contributing as one increases the laser power, and thus the gate speed [38]. The particular form of the σ^z -force allows one to take into account this term easily, finding robust pulse sequences for faster quantum gates [38]. Unfortunately, the state-dependent laser forces of this scheme (i) cannot be implemented with clock-state hyperfine qubits [39], and (ii) have some limitations for optical qubits in comparison to the entangling gates generated by σ^ϕ -forces [40]. It would be thus desirable to consider schemes to speed up entangling gates based on σ^ϕ -forces valid for both hyperfine and optical qubits. Unfortunately, the leading-order corrections to the resolved-sideband limit correspond to a time-dependent carrier driving that interferes with the σ^ϕ -force (see our discussion in section 3.2 below), and thus compromises the geometric character of the gate and the achievable fidelities.

In this work, we show that $\sigma_i^\phi \sigma_j^\phi$ -gates with higher speeds and lower errors can be achieved by exploiting the *micromotion* of ion crystals, namely a periodic motion synchronous with the oscillations of the quadrupole potential that confines the ions in a Paul trap. We consider two different types of micromotion: *excess* and *intrinsic* micromotion. Excess micromotion can be described as a classical driven motion of the ions that lie off the rf null, either due to imperfections of the trap or to crystal configurations with equilibrium positions where the rf field does not vanish. The role of this excess micromotion on entangling-gate schemes has been considered previously, showing that (i) purposely induced excess micromotion can be exploited to address different ions in a crystal via differential Rabi frequencies of secular sidebands [41]; (ii) micromotion sidebands can be exploited to increase the gate speed with respect to schemes based on secular sidebands, in situations where the excess micromotion cannot be perfectly compensated [32]; and (iii) pulse sequences for entangling gates based on

either standard normal modes [42, 43] or solitonic vibrational excitations [44], can be designed even in the presence of the excess micromotion. With the exception of [42], the role of another type of micromotion in schemes of entangling gates, namely the intrinsic micromotion, has remained largely unexplored. Intrinsic micromotion corresponds to a quantum-mechanical driven motion synchronous with the rf frequency which cannot be compensated. Being quantum-mechanical, the intrinsic micromotion has a different impact on the gate schemes. In contrast to [42], where pulsed gate schemes are used to make the performance of the gate equal to the ideal case where no micromotion is present, we explore in this work the possibility of actively exploiting the intrinsic micromotion in order to improve the gate performance, both in speed and fidelity, beyond the values of the schemes where no micromotion is considered.

This article is organized as follows. In section 2, we introduce the formalism that allows us to describe excess and intrinsic micromotion in generic ion crystals confined by Paul traps. This formalism is the starting point to develop in section 3 a general theory of laser-ion interactions in the regime of resolved sidebands in presence of both excess and intrinsic micromotion. The expressions obtained are then used to describe the main differences of the schemes that generate state-dependent dipole forces using bi-chromatic laser beams, either tuned to the secular or to the micromotion sidebands. We also describe how these forces can be used to implement entangling gates, and discuss the speed and fidelity limitations of various gate schemes, identifying a parameter regime where a gate improvement can be obtained by exploiting the intrinsic micromotion. In section 4, we discuss the possible experimental challenges in reaching such parameter regime. Finally, we present our conclusions and outlook in section 5.

2. Intrinsic and excess micromotion

In this section, we start by reviewing the classical treatment of micromotion for a single trapped ion in section 2.1. This will allow us to set the notation, and to explicitly define the notions of intrinsic and excess micromotion in ion traps. Additionally, it will provide some results that will be useful in the subsequent quantum-mechanical treatment in section 2.2. The micromotion of a trapped-ion crystal is described in section 2.3, which shall be the starting point for the scheme of micromotion-enabled improvement of quantum gates in the following section.

2.1. Classical treatment of micromotion for a single trapped ion

For the ease of exposition, we focus in this section on the electric potential configuration and micromotion effects of an ion confined in a standard linear Paul trap [6]. We note that a similar analysis would apply to segmented linear traps [45], or to surface ion traps [46], which form a key central element in various scalable architectures for QIP under development [10]. At the end of this section, we will comment on the analogies and possible differences for the micromotion in these other traps.

We consider an ion of mass M and charge Q , inside a standard linear Paul trap formed by (i) a pair of end-caps separated by a distance $2z_0$ along the trap axis (i.e. z axis), and connected to dc potentials U_0 ; (ii) four electrodes separated from the axis by a distance r_0 , and parallel to it, which are connected in pairs to either a dc potential V_0 , or an ac potential $V_0 \cos \Omega_{\text{rf}} t$, where Ω_{rf} is a fast rf frequency. Accordingly, the ion is subjected to an oscillating quadrupole potential

$$V_q = \frac{\kappa U_0}{2z_0^2} (2z^2 - (x^2 + y^2)) + \frac{V_0 \cos(\Omega_{\text{rf}} t)}{2} \left(1 + \frac{1}{r_0^2} (x^2 - y^2) \right), \quad (1)$$

where κ is a geometric factor that depends on the details of the electrodes. Here, we have assumed that the ions positions fulfill $|r| \ll r_0, z_0$, such that they lie close to the trap axis and trap center. In this way, we are neglecting corrections to the quadrupole potential, such as a small component of the alternating rf field along the direction of the trap axis.

In addition to the ideal quadrupole potential (1), there can be spurious potentials stemming from (a) potential variations due to patch effects, or to unevenly coated (charged) electrodes with elements (electrons) coming from the oven (ionization process), and (b) asymmetries in the electrode impedances [47]. The former leads to spurious dc fields \mathbf{E}_{dc} that displace the ions from the nodal line of the ac potential, whereas the latter induce small phase differences in the ac electrodes φ_{ac} , which give rise to an additional ac field. This field can be approximated by that of a pair of parallel plates connected to potentials $\pm \frac{1}{2} V_0 \varphi_{\text{ac}} \sin(\Omega_{\text{rf}} t)$, and separated by $2r_0/\tilde{\alpha}$ with $\tilde{\alpha}$ being another geometric factor that depends on the trap configuration. These spurious effects thus lead to an additional potential

$$V_s = - \left(E_{\text{dc}}^x + \frac{V_0 \varphi_{\text{ac}} \tilde{\alpha}}{2r_0} \sin(\Omega_{\text{rf}} t) \right) x - E_{\text{dc}}^y y - E_{\text{dc}}^z z. \quad (2)$$

The classical equations of motion for the ion correspond to a set of inhomogeneous Mathieu equations

$$\frac{d^2 r_\alpha}{d\tau^2} + (a_\alpha - 2q_\alpha \cos 2\tau) r_\alpha = f_\alpha(\tau), \quad \alpha \in \{x, y, z\}, \quad (3)$$

where we have introduced the dimensionless time $\tau = \frac{1}{2} \Omega_{\text{rf}} t$, and the following dimensionless parameters

$$a_x = a_y = -\frac{a_z}{2} = -\frac{4Q\kappa U_0}{Mz_0^2 \Omega_{\text{rf}}^2}, \quad q_x = -q_y = -\frac{2QV_0}{Mr_0^2 \Omega_{\text{rf}}^2}, \quad q_z = 0. \quad (4)$$

In addition, we get force terms in equation (3) due to the spurious potential (2), namely

$$f_\alpha(\tau) = \frac{4QE_{\text{dc}}^\alpha}{M\Omega_{\text{rf}}^2} + \delta_{\alpha,x} \frac{2QV_0 \varphi_{\text{ac}} \tilde{\alpha}}{Mr_0 \Omega_{\text{rf}}^2} \sin(2\tau), \quad (5)$$

where we have used the Kronecker delta $\delta_{\alpha,\beta}$ in front of the contribution that stems from the electron-impedance asymmetries, which leads to the small phase difference between the electrodes along the x -axis. The solution of these differential equations builds on the solution $r_\alpha^h(\tau)$ to the homogeneous Mathieu equation (i.e. $f_\alpha(\tau) = 0$) [48] by applying the method of variation of constants [49]. Due to the periodicity of the equation, the solution can be expressed using the Floquet theorem as follows

$$r_\alpha^h(\tau) = \sum_{n \in \mathbb{Z}} C_{2n}^\alpha (A_\alpha e^{i(\beta_\alpha + 2n)\tau} + B_\alpha e^{-i(\beta_\alpha + 2n)\tau}), \quad (6)$$

where A_α, B_α are constants that depend on the initial conditions, β_α are the so-called characteristic exponents, and C_{2n}^α are the Floquet coefficients. By substitution, one finds that these coefficients fulfill a recursion relation

$$C_{2n+2}^\alpha - D_{2n}^\alpha C_{2n}^\alpha + C_{2n-2}^\alpha = 0, \quad D_{2n}^\alpha = \frac{a_\alpha - (\beta_\alpha + 2n)^2}{q_\alpha}. \quad (7)$$

In typical experimental realizations, the parameters (4) fulfill

$$a_\alpha, q_\alpha^2 \ll 1, \quad (8)$$

and this allows one to solve the above recursion to the desired order of accuracy. To the lowest-possible order, one finds

$$\beta_\alpha = \sqrt{a_\alpha + \frac{1}{2}q_\alpha^2}, \quad C_{\pm 2\ell}^\alpha = \frac{(-1)^\ell q_\alpha^\ell C_0^\alpha}{4^\ell ((\ell - 1)!)^2}, \quad (9)$$

where we have introduced a positive integer ℓ to label the different harmonics. Note that $C_{-2\ell}^\alpha \neq C_{2\ell}^\alpha$ for general parameters. However, this difference can be neglected to leading order in the small parameters (8). Imposing that $r_\alpha(0) = r_\alpha^0$, $dr_\alpha(\tau)/d\tau|_{\tau=0} = 0$, and $C_0^\alpha = 1$, we find that the homogeneous solution describing the motion of an ion inside an ideal Paul trap is

$$r_\alpha^h(t) = \frac{r_\alpha^0}{\xi_\alpha} \cos(\omega_\alpha t) \left(1 + \sum_{\ell \geq 1} \frac{(-1)^\ell 2q_\alpha^\ell}{4^\ell ((\ell - 1)!)^2} \cos(\ell \Omega_{\text{rf}} t) \right), \quad (10)$$

where we have introduced the so-called secular frequencies

$$\omega_\alpha = \frac{\Omega_{\text{rf}}}{2} \beta_\alpha, \quad (11)$$

which are much smaller than the trap rf frequency $\omega_\alpha \ll \Omega_{\text{rf}}$. We have also introduced the parameter

$$\xi_\alpha = 1 + \sum_{\ell \geq 1} (-1)^\ell \frac{2q_\alpha^\ell}{4^\ell ((\ell - 1)!)^2}. \quad (12)$$

We can rewrite equation (10) as $r_\alpha^h(t) = r_\alpha^{\text{sec}}(t) + r_\alpha^{\text{in}}(t)$, such that the ion in an ideal Paul trap displays slow oscillations at the secular frequency described by

$$r_\alpha^{\text{sec}}(t) = \frac{r_\alpha^0}{\xi_\alpha} \cos(\omega_\alpha t), \quad (13)$$

accompanied by smaller and faster oscillations synchronous with the ac potential

$$r_\alpha^{\text{in}}(t) = r_\alpha^{\text{sec}}(t) \left(\sum_{\ell \geq 1} \frac{(-1)^\ell 2q_\alpha^\ell}{4^\ell ((\ell - 1)!)^2} \cos(\ell \Omega_{\text{rf}} t) \right). \quad (14)$$

These smaller oscillations are referred to as *micromotion*, and occur roughly at multiples of the rf frequency $\ell\Omega_{\text{rf}}$ (i.e. micromotion sidebands). To distinguish this behavior from the one stemming from the spurious potential (2), these fast oscillations $r_{\alpha}^{\text{in}}(t)$ are sometimes referred to as *intrinsic micromotion* [50], to highlight the fact that such a motion is intrinsic to the oscillating quadrupole of an Paul trap, even for an ideal trap design without any imperfection (2).

The solution to the forced Mathieu equation (3) can be found using the method of variation of constants with the two independent solutions associated to equation (6), namely $r_{\alpha}^{\text{h}}(t) = A_{\alpha}r_{\alpha,1}(t) + B_{\alpha}r_{\alpha,2}(t)$. The complete solution is

$$r_{\alpha}(t) = r_{\alpha}^{\text{sec}}(t) + r_{\alpha}^{\text{in}}(t) + r_{\alpha}^{\text{ex}}(t), \quad (15)$$

where the additional part due to the spurious potential is

$$r_{\alpha}^{\text{ex}}(t) = \int d\tau' \frac{(r_{\alpha,2}(\tau)r_{\alpha,1}(\tau') - r_{\alpha,1}(\tau)r_{\alpha,2}(\tau'))f_{\alpha}(\tau')}{\mathbb{W}_{\alpha}(\tau')}, \quad (16)$$

and $\mathbb{W}_{\alpha}(\tau') = r_{\alpha,1}(\tau')dr_{\alpha,2}(\tau')/d\tau' - r_{\alpha,2}(\tau')dr_{\alpha,1}(\tau')/d\tau'$ is the Wronskian of the two solutions, which can be shown to be constant in this case $\mathbb{W}(\tau') = -2i\beta_{\alpha}$. When performing the integrals, we keep only the slowly varying terms, which give rise to the leading-order solution

$$r_{\alpha}^{\text{ex}}(t) = r_{\alpha}^{\text{driv}}(t) \left(1 + \sum_{\ell \geq 1} \frac{(-1)^{\ell} 2q_{\alpha}^{\ell}}{4^{\ell} ((\ell - 1)!)^2} \cos(\ell\Omega_{\text{rf}}t) \right), \quad (17)$$

where we have introduced the following driven amplitude

$$r_{\alpha}^{\text{driv}}(t) = \frac{QE_{\text{dc}}^{\alpha}}{M\omega_{\alpha}^2} + \delta_{\alpha,x} \frac{q_x r_0 \varphi_{\text{ac}} \tilde{\alpha}}{4} \sin(\Omega_{\text{rf}}t). \quad (18)$$

We thus observe that the spurious potential (2) induces a driven motion (17) that is also synchronous with the rf frequency, and is thus another type of micromotion. Since it is not linked to the secular motion, and can only be reduced by compensating the spurious potential terms (2), this motion is usually referred to as *excess micromotion* [47]. Along this text, we will use the wording micromotion compensation to refer to the compensation of the stray fields that produce excess micromotion.

As a consistency check, we note that to linear order in q_{α} , the complete solution (15) built from equations (13), (14) and (17) coincides with the solution presented in [47], which includes the secular motion and the first micromotion sideband. The higher-order powers of q_{α} allow us to account for all higher micromotion sidebands. Note also that the intrinsic (14) and excess (17) micromotion only occur in those trap axes where $q_{\alpha} \neq 0$. According to equation (4), micromotion in an ideal linear Paul trap only occurs in the transverse directions, as there is no rf field along the axial direction, such that $q_z = 0$. However, for realistic experimental conditions that depart from this ideal case, there might also be axial micromotion $q_z \neq 0$, as occurs for instance in segmented linear traps [50]. Accordingly, we will consider the most general case, and allow for micromotion in all possible directions $q_{\alpha} \neq 0, \forall \alpha \in \{x, y, z\}$. The particular microscopic expression of these parameters will generally differ from equation (4), and depend on specific details of the trap. For the excess micromotion (17), the driven amplitude $r_{\alpha}^{\text{driv}}(t)$ will differ from the ideal case (18), and also depend on specific details of the trap. However, one can treat the micromotion generically using equations (13), (14) and (17), with generic parameters $r_{\alpha}^{\text{driv}}(t)$, a_{α} , q_{α} only restricted to fulfill equation (8).

2.2. Quantum-mechanical treatment of micromotion for a single trapped ion

Since the ultimate goal of this work is to exploit the micromotion to improve phonon-mediated quantum logic gates between distant trapped-ion qubits, a full quantum-mechanical treatment of the secular vibrations and the intrinsic/excess micromotion in a trapped-ion crystal will be required. A detailed quantum-mechanical treatment of the secular vibrations and intrinsic micromotion for a single trapped ion has been described in [6] using a formalism based on quantum-mechanical constants of motion [51]. We now use this formalism to generalize the description to situations where excess micromotion of a single trapped ion is also present.

The quantum-mechanical Hamiltonian of the ion inside the Paul trap can be described as

$$H = \sum_{\alpha} \left(\frac{1}{2M} \hat{p}_{\alpha}^2 + \frac{1}{2} K_{\alpha}(t) \hat{r}_{\alpha}^2 - M F_{\alpha}(t) \hat{r}_{\alpha} \right), \quad (19)$$

where we have promoted the position and momentum to quantum-mechanical operators fulfilling $[\hat{r}_{\alpha}, \hat{p}_{\beta}] = i\delta_{\alpha,\beta}$. Here, we have introduced a time-dependent spring constant

$$K_{\alpha}(t) = \frac{M}{4} \Omega_{\text{rf}}^2 (a_{\alpha} - 2q_{\alpha} \cos \Omega_{\text{rf}}t), \quad (20)$$

and used the time-dependent forces (5) caused by the deviations (2) from an ideal Paul trap, transformed back into real time

$$F_\alpha(t) = \frac{1}{4}\Omega_{\text{rf}}^2 f_\alpha\left(\frac{1}{2}\Omega_{\text{rf}}t\right). \quad (21)$$

The Heisenberg equations of motion for this Hamiltonian lead to a quantum-mechanical version of the classical forced Mathieu equations (3) for the position operator, namely

$$\frac{d^2\hat{r}_\alpha(t)}{dt^2} + \frac{K_\alpha(t)}{M}\hat{r}_\alpha(t) = F_\alpha(t), \quad \alpha \in \{x, y, z\}. \quad (22)$$

We now construct an operator constant of motion by combining the position operator $\hat{r}_\alpha(t)$ fulfilling equation (22), with a mode function $u_\alpha(t)$ that evolves according to the solution of the homogeneous classical Mathieu equation (6), but with initial conditions $u_\alpha(0) = 1$, $du_\alpha(t)/dt|_{t=0} = i\omega_\alpha$, and $C_0^\alpha = 1$. This generalizes the standard mode function $u_\alpha^{\text{st}}(t) = e^{i\omega_\alpha t}$ that appears in the Heisenberg picture of a time-independent harmonic oscillator of frequency ω_α , and can be expressed as follows

$$u_\alpha(t) = \frac{e^{i\omega_\alpha t}}{\xi_\alpha} \left(1 + \sum_{\ell \geq 1} \frac{(-1)^\ell 2q_\alpha^\ell}{4^\ell ((\ell-1)!)^2} \cos(\ell\Omega_{\text{rf}}t) \right), \quad (23)$$

where we used the secular frequencies (11) and the normalization (12). The operator constant of motion is built from the Wronskian of the position operator and the mode function

$\widehat{\mathbb{W}}_\alpha(t) = u_\alpha(t)d\hat{r}_\alpha(t)/dt - \hat{r}_\alpha(t)du_\alpha(t)/dt$, namely

$$a_\alpha(t) = i\sqrt{\frac{M}{2\omega_\alpha}} \left(\widehat{\mathbb{W}}_\alpha(t) - \int_0^t dt' u_\alpha(t') F_\alpha(t') \right), \quad (24)$$

which fulfills $a_\alpha(t) = a_\alpha$, where

$$a_\alpha = \sqrt{\frac{M\omega_\alpha}{2}} \left(\hat{r}_\alpha + \frac{i}{M\omega_\alpha} \hat{p}_\alpha \right) \quad (25)$$

is the standard annihilation operator of a harmonic oscillator vibrating at the secular frequency. Using these expressions, and keeping once more the slowly varying terms under the integral of equation (23), we find that the quantum-mechanical position operator can be expressed as follows

$$\hat{r}_\alpha(t) = \hat{r}_\alpha^{\text{sec}}(t) + \hat{r}_\alpha^{\text{in}}(t) + r_\alpha^{\text{ex}}(t)\hat{\mathbb{I}}. \quad (26)$$

Here, the secular-motion position operator is given by

$$\hat{r}_\alpha^{\text{sec}}(t) = \frac{1}{\sqrt{2M\omega_\alpha}} \frac{1}{\xi_\alpha} (a_\alpha^\dagger e^{i\omega_\alpha t} + a_\alpha e^{-i\omega_\alpha t}). \quad (27)$$

The intrinsic micromotion operator can be expressed as

$$\hat{r}_\alpha^{\text{in}}(t) = \hat{r}_\alpha^{\text{sec}}(t) \left(\sum_{\ell \geq 1} \frac{(-1)^\ell 2q_\alpha^\ell}{4^\ell ((\ell-1)!)^2} \cos(\ell\Omega_{\text{rf}}t) \right), \quad (28)$$

and is thus again proportional to the secular motion, as occurred in the classical case (14). Since the secular motion is expressed in terms of quantum-mechanical creation-annihilation operators, the intrinsic micromotion can be argued to be a quantum-mechanical motion synchronous with the rf oscillating field, as we advanced in the introduction of this work. As a consistency check, we note that to linear order in q_α , we recover the expressions described in [6].

Finally, equation (26) also includes the effects of excess micromotion in the position operator, which are proportional to the identity operator in the vibrational Hilbert space $\hat{\mathbb{I}}$. As expected from the forces in equation (19), the excess micromotion corresponds to a simple displacement over the position operator $\hat{r}_\alpha^{\text{sec}}(t) \rightarrow \hat{r}_\alpha^{\text{sec}}(t) + r_\alpha^{\text{driv}}(t)\hat{\mathbb{I}}$, the magnitude of which coincides exactly with the classical driven amplitude (18). One thus finds that the deviations from an ideal Paul trap affect the quantum-mechanical position operator (26) through the classical expression $r_\alpha^{\text{ex}}(t)$ of the excess micromotion (17). Accordingly, the excess micromotion can be considered as a classical driven motion that can indeed be compensated by minimizing the spurious terms (2), in contrast to the intrinsic micromotion.

2.3. Quantum-mechanical treatment of micromotion in a trapped-ion crystal

The standard treatment of phonons in solids considers small quantized displacements of the ions $\delta\hat{r}_{i,\alpha}$ with respect to an underlying Bravais lattice $r_{i,\alpha}^0$, namely $\hat{r}_{i,\alpha}(t) = r_{i,\alpha}^0 + \delta\hat{r}_{i,\alpha}$, where $i \in \{1, \dots, N\}$ labels a particular ion. The collective modes of vibration, whose quantum-mechanical excitations lead to the aforementioned phonons, are usually obtained in the harmonic approximation by expanding the inter-ionic potential to second

order in the displacements, and diagonalising the resulting quadratic Hamiltonian [52]. For a collection of N ions inside a Paul trap, an analogous treatment exists in the so-called pseudo-potential approximation, which assumes that the ions are effectively trapped by a time-independent quadratic potential with secular trap frequencies (11). The main difference with respect to a solid is that the equilibrium positions $r_{i\alpha}^0$ do not correspond to a Bravais lattice, but instead form an inhomogeneous array known as a Coulomb crystal [53]. This approximation, however, does not include possible effects of micromotion in the ion crystal.

A careful classical treatment of the crystal micromotion [54] has recently shown that it can have non-trivial effects, such as a renormalization of the normal-mode frequencies in planar crystals [55]. We now present a detailed quantum-mechanical treatment of both the intrinsic and excess micromotion in ion crystals, which combines the techniques presented in section 2.1 with the formalism in [54] to describe the effect of micromotion on the classical crystal, and then generalizes section 2.2 to describe quantum-mechanically the effect of micromotion on the phonons of the ion crystal.

To incorporate the different types of micromotion introduced above, we generalize the quantum-mechanical Hamiltonian (19) to a system of N ions confined by an oscillating quadrupole

$$H = \sum_{i,\alpha} \left(\frac{\hat{p}_{i,\alpha}^2}{2M} + \frac{1}{2} K_\alpha(t) \hat{r}_{i,\alpha}^2 - M F_{i,\alpha}(t) \hat{r}_{i,\alpha} \right) + \sum_{i,j} \frac{\tilde{Q}^2}{2|\hat{r}_i - \hat{r}_j|}, \quad (29)$$

where we have introduced vectorial operators defined in terms of the unit cartesian vectors $\hat{r}_i = \sum_\alpha \hat{r}_{i,\alpha} \mathbf{e}_\alpha$, and the position-momentum operators now fulfill $[\hat{r}_{i,\alpha}, \hat{p}_{j,\beta}] = i\delta_{\alpha,\beta}\delta_{ij}$. Here, $\tilde{Q}^2 = Q^2/4\pi\epsilon_0$ eases notation, and we have used the spring constants (20) and time-dependent forces (21) introduced above, allowing the spurious dc fields in equation (5) to be inhomogeneous along the crystal. The Heisenberg equations of motion lead to a system of equations

$$\frac{d^2 \hat{r}_{i,\alpha}}{dt^2} + \frac{K_\alpha(t)}{M} \hat{r}_{i,\alpha} - \tilde{Q}^2 \sum_{j \neq i} \frac{\hat{r}_{i,\alpha} - \hat{r}_{j,\alpha}}{|\hat{r}_i - \hat{r}_j|^3} = F_{i,\alpha}(t). \quad (30)$$

Paralleling the standard treatment of phonons in solids, we substitute

$$\hat{r}_{i,\alpha} \rightarrow r_{i,\alpha}^0(t) \hat{\mathbb{I}} + \delta \hat{r}_{i,\alpha}, \quad (31)$$

where $r_{i,\alpha}^0(t)$ are the equivalent of the equilibrium positions in solids, which become time-dependent quantities in the presence of micromotion (i.e. breathing crystal), and $\delta \hat{r}_{i,\alpha}$ are the small quantized vibrations around such a breathing crystal. When these vibrations are sufficiently small, the equations (30) decouple into (i) a classical system of differential equations for the coordinates of the breathing crystal, and (ii) a linear system of equations for the quantum-mechanical displacements.

Let us focus on (i), and rescale the time $\tau = \frac{1}{2}\Omega_{\text{rf}} t$, such that the time-periodic breathing crystal fulfills

$$\frac{d^2 r_{i,\alpha}^0}{d\tau^2} + (a_\alpha - 2q_\alpha \cos 2\tau) r_{i,\alpha}^0 - \frac{4\tilde{Q}^2}{M\Omega_{\text{rf}}^2} \sum_{j \neq i} \frac{r_{i,\alpha}^0 - r_{j,\alpha}^0}{|r_i^0 - r_j^0|^3} = 0. \quad (32)$$

These differential equations correspond to a system of coupled Mathieu equations (3) and, inspired by the previous section, we thus propose a Floquet-type ansatz the form of equation (6), namely

$$r_{i,\alpha}^0(\tau) = \sum_{n \in \mathbb{Z}} C_{2n,i}^\alpha (A_\alpha e^{i(\beta_\alpha + 2n)\tau} + B_\alpha e^{-i(\beta_\alpha + 2n)\tau}), \quad (33)$$

where A_α, B_α are constants that depend on the initial conditions, β_α is the so-called characteristic exponent, and $C_{2n,i}^\alpha$ are the Floquet coefficients. The breathing crystal corresponds to a classical solution of the type (33) synchronous with the rf potential, i.e. $\beta_\alpha = 0$, and can also be considered as part of the excess micromotion due to ion positions lying off the rf null. By substituting this expression (33) in equation (32), one observes that the Coulomb repulsion can introduce higher harmonics of the rf frequency. For the linear ion crystals of interest to our purposes, these effects are absent in the relevant parameter regime (8), where the Floquet coefficients fulfill a system of coupled recursion relations

$$C_{2n+2,i}^\alpha - D_{2n}^\alpha C_{2n,i}^\alpha - \sum_{j \neq i} \frac{\zeta (C_{2n,i}^\alpha - C_{2n,j}^\alpha)}{\left[\sum_\alpha (C_{0,i}^\alpha - C_{0,j}^\alpha)^2 \right]^{\frac{3}{2}}} + C_{2n-2,i}^\alpha = 0. \quad (34)$$

Here, we have used the same notation as in the recursion relation for a single ion (7), $D_{2n}^\alpha = (a_\alpha - 4n^2)/q_\alpha$, and introduced the parameter $\zeta = 4\tilde{Q}^2/M\Omega_{\text{rf}}^2 q_\alpha$. To the lowest possible order in (8), one finds that all the Floquet coefficients

$$C_{\pm 2\ell,i}^\alpha = \frac{(-1)^\ell q_\alpha^\ell C_{0,i}^\alpha}{4^\ell ((\ell - 1)!)^2} \quad (35)$$

are expressed in terms of the time-independent one $C_{0,i}^\alpha$. This coefficient is in turn determined by the solutions of the following system of algebraic equations

$$M\omega_\alpha^2 C_{0,i}^\alpha - \sum_{j \neq i} \frac{\tilde{Q}^2 (C_{0,i}^\alpha - C_{0,j}^\alpha)}{\left[\sum_\alpha (C_{0,i}^\alpha - C_{0,j}^\alpha)^2 \right]^{\frac{3}{2}}} = 0, \quad (36)$$

where we have made use of the secular trapping frequencies introduced in equation (11). Let us note that these equations display a clear competition between the harmonic trapping and the Coulomb repulsion, and coincide with those that determine the equilibrium positions of the ion crystal in the pseudo-potential approximation [53]. Therefore, we shall denote the solutions as $r_{i,\alpha}^{\text{eq}} = C_{0,i}^\alpha$, which can be found numerically.

Since we are interested in the linear-trap configuration $\omega_z \ll \omega_x, \omega_y$, where $r_{i,\alpha}^{\text{eq}} = z_i^0 \delta_{\alpha,z}$, and the oscillating quadrupole has no effect along the trap axis of an ideal Paul trap $q_z = 0$; we find that $C_{\pm 2\ell,i}^\alpha = 0, \forall \ell \geq 1$ at this leading order. In fact, only terms at a higher-power of the non-vanishing parameters q_x, q_y can lead to corrections [54], but these are negligible in the regime of equation (8). Accordingly, the time-periodic breathing crystal (33) in an ideal Paul trap corresponds to a static Coulomb crystal

$$\mathbf{r}_i^0(t) = z_i^0 \mathbf{e}_z. \quad (37)$$

In a segmented linear trap, where residual axial micromotion may exist $0 < q_z \ll q_x, q_y$, one would still obtain a static crystal to leading order. Conversely, for crystalline solutions where ions lie off the trap axis, the higher-order harmonics introduced by the Coulomb interaction in equation (32) for a breathing crystal with $q_x, q_y > 0$ must be considered in detail for an accurate description [54, 55].

Given this solution (37), we can now turn our attention onto (ii), namely the quantum-mechanical displacements about the crystal. After linearization, one can show that the corresponding operators evolve according to a system of forced Mathieu equations, similar to the single-ion case (22), but now coupled via the linearized Coulomb interaction

$$\frac{d^2}{dt^2} \delta \hat{r}_{i,\alpha}(t) + \sum_j \frac{\mathbb{K}_{ij}^\alpha(t)}{M} \delta \hat{r}_{j,\alpha}(t) = F_{i,\alpha}(t), \quad (38)$$

where we have now time-dependent spring constants that couple distant ions

$$\mathbb{K}_{ij}^\alpha(t) = \delta_{i,j} K_\alpha(t) + \mathbb{V}_{ij}^\alpha(t). \quad (39)$$

Here, we have used the single-ion spring constants (20), and introduced the matrix of Coulomb-mediated couplings

$$\mathbb{V}_{ij}^\alpha(t) = \frac{(1 - \delta_{i,j}) \tilde{Q}^2}{|\mathbf{r}_i^0(t) - \mathbf{r}_j^0(t)|^3} (\delta_{\alpha,x} + \delta_{\alpha,y} - 2\delta_{\alpha,z}) - \sum_{\ell \neq i} \frac{\delta_{i,j} \tilde{Q}^2}{|\mathbf{r}_i^0(t) - \mathbf{r}_\ell^0(t)|^3} (\delta_{\alpha,x} + \delta_{\alpha,y} - 2\delta_{\alpha,z}). \quad (40)$$

For the linear crystals (37) that concern us in this work, this coupling matrix becomes time-independent $\mathbb{V}_{ij}^\alpha(t) = \mathbb{V}_{ij}^\alpha$, and the system of differential equations can be decoupled by a single orthogonal transformation, in analogy to the standard theory of phonons in solids [52]. We thus introduce the following normal-mode operators

$$\hat{R}_{m,\alpha}(t) = \sum_i \mathcal{M}_{i,m}^\alpha \delta \hat{r}_{i,\alpha}(t), \quad \hat{P}_{m,\alpha}(t) = \sum_i \mathcal{M}_{i,m}^\alpha \hat{p}_{i,\alpha}(t), \quad (41)$$

where the orthogonal matrix is determined by diagonalizing the matrix of Coulomb-mediated couplings

$$\sum_{i,j} \mathcal{M}_{i,n}^\alpha \mathbb{V}_{ij}^\alpha \mathcal{M}_{j,m}^\alpha = \delta_{n,m} \mathcal{V}_m^\alpha, \quad (42)$$

where we have introduced the eigenvalues \mathcal{V}_m^α . Using the orthogonality of the transformation, we find a set of decoupled forced Mathieu equations for the normal-mode operators

$$\frac{d^2}{dt^2} \hat{R}_{m,\alpha}(t) + \frac{\kappa_m^\alpha(t)}{M} \hat{R}_{m,\alpha}(t) = \mathfrak{F}_{m,\alpha}(t). \quad (43)$$

Here, the eigenvalues of the spring-coupling matrix

$$\kappa_m^\alpha(t) = K_\alpha(t) + \mathcal{V}_m^\alpha \quad (44)$$

inherit the time-dependence via the single-ion spring constants (20), and we have introduced forces that tend to displace the ions along the normal-mode directions

$$\mathfrak{F}_{m,\alpha}(t) = \sum_i \mathcal{M}_{i,m}^\alpha \tilde{F}_{i,\alpha}(t). \quad (45)$$

Hence, we have reduced the dynamics of the small quantum displacements about the crystalline solution into $3N$ instances of the single-ion problem (22). We must thus find $3N$ operators that are constants of motion,

which requires finding a set of normal mode functions $u_{m,\alpha}(t)$ that are solutions of the homogeneous Mathieu equations (43), namely

$$u_{m,\alpha}(t) = \sum_{n \in \mathbb{Z}} C_{2n,m}^\alpha (A_{m,\alpha} e^{i(\beta_{m,\alpha} + 2n)\frac{\Omega_{\text{rf}} t}{2}} + B_{m,\alpha} e^{-i(\beta_{m,\alpha} + 2n)\frac{\Omega_{\text{rf}} t}{2}}). \quad (46)$$

This is the generalization of equation (6) with constants $A_{m,\alpha}$, $B_{m,\alpha}$ that depend on the initial conditions, characteristic exponents for each normal mode $\beta_{m,\alpha}$, and Floquet coefficients $C_{2n,m}^\alpha$. We impose the initial conditions $u_{m,\alpha}(0) = 1$, $du_{m,\alpha}(t)/dt|_{t=0} = i\omega_{m,\alpha}$, and $C_{0,m}^\alpha = 1$, such that the mode functions to leading order in (8) can be expressed as

$$u_{m,\alpha}(t) = \frac{e^{i\omega_{m,\alpha} t}}{\xi_\alpha} \left(1 + \sum_{\ell \geq 1} \frac{(-1)^\ell 2q_\alpha^\ell}{4^\ell ((\ell - 1)!)^2} \cos(\ell \Omega_{\text{rf}} t) \right), \quad (47)$$

with the normalization constant defined in equation (12), and the normal-mode secular frequencies

$$\omega_{m,\alpha} = \sqrt{\omega_\alpha^2 + \mathcal{V}_m^\alpha}, \quad (48)$$

where we have used the secular frequency in equation (11).

Given these normal-mode functions, one can obtain the Wronskian and the constants of motion through a straightforward generalization of equation (24) by introducing the annihilation operators for each collective vibrational mode

$$a_{m,\alpha} = \sqrt{\frac{M\omega_{m,\alpha}}{2}} \left(\hat{R}_{m,\alpha} + \frac{i}{M\omega_{m,\alpha}} \hat{P}_{m,\alpha} \right). \quad (49)$$

Therefore, the analog of equation (26) for the quantum-mechanical treatment of micromotion in a trapped-ion crystal can be expressed as

$$\hat{r}_{i,\alpha}(t) = r_{i,\alpha}^0(t) \hat{\mathbb{I}} + \delta \hat{r}_{i,\alpha}^{\text{sec}}(t) + \delta \hat{r}_{i,\alpha}^{\text{in}}(t) + r_{i,\alpha}^{\text{ex}}(t) \hat{\mathbb{I}}. \quad (50)$$

Here, the secular-motion position operator is given by

$$\delta \hat{r}_{i,\alpha}^{\text{sec}}(t) = \sum_m \frac{\mathcal{M}_{i,m}^\alpha}{\sqrt{2M\omega_{m,\alpha}} \xi_\alpha} \frac{1}{\xi_\alpha} (a_{m,\alpha}^\dagger e^{i\omega_{m,\alpha} t} + a_{m,\alpha} e^{i\omega_{m,\alpha} t}), \quad (51)$$

and the intrinsic micromotion operator can be expressed as

$$\delta \hat{r}_{i,\alpha}^{\text{in}}(t) = \delta \hat{r}_{i,\alpha}^{\text{sec}}(t) \left(\sum_{\ell \geq 1} \frac{(-1)^\ell 2q_\alpha^\ell}{4^\ell ((\ell - 1)!)^2} \cos(\ell \Omega_{\text{rf}} t) \right). \quad (52)$$

The excess micromotion in equation (50) is expressed in terms of the identity operator in the vibrational Hilbert space $\hat{\mathbb{I}}$, and

$$r_{i,\alpha}^{\text{ex}}(t) = r_{i,\alpha}^{\text{driv}}(t) \left(1 + \sum_{\ell \geq 1} \frac{(-1)^\ell 2q_\alpha^\ell}{4^\ell ((\ell - 1)!)^2} \cos(\ell \Omega_{\text{rf}} t) \right), \quad (53)$$

where we have introduced the generic site-dependent amplitude $r_{i,\alpha}^{\text{driv}}(t)$. For the standard Paul trap, this can be obtained from equation (18) by considering inhomogeneous spurious fields

$$r_{i,\alpha}^{\text{driv}}(t) = \frac{QE_{\text{dc},i}^\alpha}{M\omega_\alpha^2} + \delta_{\alpha,x} \frac{q_x r_0 \varphi_{\text{ac}} \tilde{\alpha}}{4} \sin(\Omega_{\text{rf}} t). \quad (54)$$

For other situations, such as those arising for segmented traps, this amplitude will depend on the specific trap details.

In this way, we have presented a detailed quantum-mechanical description of the effects of intrinsic and excess micromotion in a linear crystal of trapped ions. The results in equations (50)–(54) will be the starting point for the scheme of micromotion-enabled entangling gates in the following section. Our formalism can be extended to planar crystals, although one has to consider the breathing of the crystal instead of equation (37), and how this can lead to micromotion-induced corrections of the secular vibrations of the planar crystal.

3. Entangling gates based on micromotion sidebands

In this section, we start in section 3.1 by discussing the effects of micromotion in the theory of light–matter interactions for a set of laser beams addressed to a particular electronic transition of the ions. We then describe how to implement state-dependent forces by combining pairs of laser beams in section 3.2, and discuss the role of intrinsic/excess micromotion, paying special attention to the contribution of the often-neglected carrier

excitations. In section 3.3, we start by reviewing the schemes for entangling gates based on secular state-dependent σ^ϕ -forces [28, 29–32], and discussing the gate speed limitations that arise due to the off-resonant carrier. Building on this discussion, we then introduce a scheme of micromotion-enabled state-dependent σ^ϕ -forces, which can overcome the limitations on the gate speed due to the off-resonant carrier, provided that the excess micromotion is accurately compensated.

3.1. Micromotion effects in the laser-ion interaction

Let us consider a collection of N trapped ions subjected to laser beams tuned close to the resonance of a particular transition of frequency ω_0 between two electronic levels $|\uparrow_i\rangle, |\downarrow_i\rangle$. The dynamics of the internal and motional degrees of freedom of this ion crystal is described by the following Hamiltonian

$$H_0(t) = \sum_i \frac{\omega_0}{2} \sigma_i^z + \sum_{i,\alpha} \left(\frac{\hat{p}_{i,\alpha}^2}{2M} + \frac{1}{2} K_\alpha(t) \delta \hat{r}_{i,\alpha}^2 - M F_{i,\alpha}(t) \delta \hat{r}_{i,\alpha} + \sum_j \nabla_{ij}^\alpha \delta \hat{r}_{i,\alpha} \delta \hat{r}_{j,\alpha} \right), \quad (55)$$

where we have introduced $\sigma_i^z = |\uparrow_i\rangle\langle\uparrow_i| - |\downarrow_i\rangle\langle\downarrow_i|$, applied the harmonic-crystal approximation described in the previous section (31), and neglected an irrelevant c -number stemming from the classical energy of the breathing crystal. The interaction between the laser beams and the ions is described by

$$H_1(t) = \sum_{i,l} \frac{\Omega_l}{2} e^{i\phi_l} \sigma_i^\pm e^{i(\mathbf{k}_l \cdot \hat{\mathbf{r}}_i(t) + (\omega_0 - \omega_l)t)} + \text{h.c.}, \quad (56)$$

where we have introduced the spin raising $\sigma_i^+ = |\uparrow_i\rangle\langle\downarrow_i|$ and lowering $\sigma_i^- = |\downarrow_i\rangle\langle\uparrow_i|$ operators. Here, l labels the different laser beams that are described as classical traveling waves with $\mathbf{k}_l, \omega_l, \phi_l$ being the laser wavevector, frequency, and phase, respectively, and Ω_l is the Rabi frequency of the particular transition.

Typically, one either considers a quadrupole-allowed transition between a groundstate level $|\downarrow\rangle$ and a metastable excited level $|\uparrow\rangle$, or uses a two-photon Raman scheme to couple a pair of groundstate levels $|\downarrow\rangle, |\uparrow\rangle$ via a excited level through a far-off-resonant dipole transition. In any case, the quadrupole or Raman Rabi frequencies are constrained to $|\Omega_l| \ll \omega_0 + \omega_l$ in order to neglect additional counter-rotating terms in equation (56).

We note that this expression is obtained in the interaction picture of the bare Hamiltonian (55), namely $H_1(t) = U_0^\dagger(t) H_1 U_0(t)$, where $U_0(t) = \mathcal{T} \{ \exp(-i \int_0^t dt' H_0(t')) \}$. Thus, after substituting the position operator in equations (50)–(54) corresponding to such an interaction picture, we find

$$H_1(t) = \sum_{i,l,\alpha} \frac{\Omega_{li}^\alpha}{2} \sigma_i^\pm \left(1 + i \sum_m \mathcal{M}_{i,m}^\alpha \eta_{l,m}^\alpha (a_{m,\alpha}^\dagger u_{m,\alpha}(t) + a_{m,\alpha} u_{m,\alpha}^*(t)) + \dots \right) e^{i\phi_{li}(t)} e^{i(\omega_0 - \omega_l)t} + \text{h.c.}, \quad (57)$$

where we have performed a Taylor series in the Lamb–Dicke parameters $\eta_{l,m}^\alpha = \mathbf{k}_l \cdot \mathbf{e}_\alpha / \sqrt{2M\omega_{m,\alpha}} \ll 1$, and introduced the renormalised Rabi frequencies $\Omega_{li}^\alpha = \Omega_l \exp\{-\sum_m (\mathcal{M}_{i,m}^\alpha \eta_{l,m}^\alpha)^2 / 2\}$, together with laser phases that get modulated by the time-dependence of the breathing crystal and the excess micromotion

$$\phi_{l,i}(t) = \phi_l + \mathbf{k}_l \cdot (\mathbf{r}_i^0(t) + \mathbf{r}_i^{\text{ex}}(t)). \quad (58)$$

Note that for a linear chain, the breathing crystal becomes static $\mathbf{r}_i^0(t) = z_i^0 \mathbf{e}_z$ (37), such that the phase modulation is only caused by the excess micromotion. Additionally, the effect of the intrinsic micromotion on the laser-ion interaction is encoded in the particular time-dependence of the mode functions $u_{m,\alpha}(t)$ (47), which yield additional periodic modulations in processes involving the creation and annihilation of phonons.

Let us note that the mode functions are written in equation (47) as $u_{m,\alpha}(t) = e^{i\omega_{m,\alpha} t} f_{\text{in}}^\alpha(t)$, where $f_{\text{in}}^\alpha(t)$ is a function with period $2\pi/\Omega_{\text{rf}}$ already written as a Fourier series. The excess micromotion leads to $f_{\text{ex}}^l(t) = e^{i\phi_{li}(t)}$, which is also a periodic function with period $2\pi/\Omega_{\text{rf}}$, and could as well be expressed as a Fourier series with all the possible harmonics at the different frequencies $\ell \Omega_{\text{rf}}$. In this sense, the micromotion introduces a comb of equidistant sidebands in the laser-ion interaction (57), the so-called *micromotion sidebands*. These can be exploited by choosing an appropriate detuning of the lasers with respect to the atomic transition

$$\omega_l - \omega_0 \approx \ell_* \Omega_{\text{rf}}, \quad (59)$$

where $\ell_* \in \mathbb{Z}$ is a certain integer. In most trapped-ion experiments, one sets $\ell_* = 0$ [5], and compensates the excess micromotion in order to minimize its effects [47]. The main result of this work is to point out that addressing the first micromotion sideband $\ell_* = 1$, while maintaining the compensation of excess micromotion, can be advantageous for QIP. In this way, one can exploit the effects of intrinsic micromotion in the laser-ion interaction, and find faster and more accurate schemes for entangling quantum logic gates.

3.2. State-dependent dipole forces and off-resonant carriers

We now discuss how to induce a state-dependent σ^ϕ -force [28] on the ions starting from equation (57), and thus taking into account the new effects brought forth by micromotion. We consider a pair of laser beams $l \in \{1, 2\}$

with equal wavevectors $\mathbf{k}_1 = \mathbf{k}_2 := \mathbf{k}_L$. By selecting the direction of these beams along a certain trap axis $\mathbf{k}_L || \mathbf{e}_\alpha$, the laser-ion interaction will only couple the qubits to a particular phonon branch.

We also consider equal laser phases $\phi_1 = \phi_2 := \phi$, and equal intensities and polarizations leading to $\Omega_1 = \Omega_2 := \Omega$. Conversely, the lasers will have opposite detunings with respect to the atomic transition $\delta := \omega_1 - \omega_0 = -(\omega_2 - \omega_0)$. Due to these choices, we can simplify the laser-ion interaction (57) considerably by defining common Lamb–Dicke parameters $\eta_{1,n}^\alpha = \eta_{2,n}^\alpha := \eta_n^\alpha$, dressed Rabi frequencies $\Omega_{1,i}^\alpha = \Omega_{2,i}^\alpha := \Omega_i^\alpha$, and modulated phases $\phi_{1,i}(t) = \phi_{2,i}(t) := \phi_i(t)$, where

$$\phi_i(t) = \phi + k_L r_{i,\alpha}^0 + k_L r_{i,\alpha}^{\text{driv}}(t) \left(1 + \sum_{\ell \geq 1} \frac{(-1)^\ell 2q_\alpha^\ell \cos(\ell \Omega_{\text{rf}} t)}{4^\ell ((\ell - 1)!)^2} \right). \quad (60)$$

By keeping contributions to first order in the Lamb–Dicke parameter, $H_1(t) = H_c(t) + H_s(t)$, we identify the terms driving the carrier transitions

$$H_c(t) = \sum_i \Omega_i^\alpha \sigma_i^+ e^{i\phi_i(t)} \cos \delta t + \text{h.c.}, \quad (61)$$

and the spin-phonon couplings

$$H_s(t) = \sum_{i,m} i \mathfrak{F}_{i,m}^\alpha x_m^\alpha (a_{m,\alpha}^\dagger u_{m,\alpha}(t) + \text{H.c.}) \sigma_i^+ e^{i\phi_i(t)} \cos \delta t + \text{h.c.}, \quad (62)$$

where the dipole forces are $\mathfrak{F}_{i,m}^\alpha = \Omega_i^\alpha \mathcal{M}_{i,m}^\alpha k_L$, and the n th mode groundstate widths are $x_m^\alpha = 1/\sqrt{2M\omega_{m,\alpha}}$.

We now consider the effects of the excess micromotion (60) to leading order in the regime (8), namely

$$\phi_i(t) \approx \varphi_i + \tilde{\beta}_i \cos(\Omega_{\text{rf}} t), \quad (63)$$

where we have introduced the parameters

$$\varphi_i = \phi + k_L (r_{i,\alpha}^0 + r_{i,\alpha}^{\text{driv}}(0)), \quad \tilde{\beta}_i = -k_L r_{i,\alpha}^{\text{driv}}(0) \frac{q_\alpha}{2}. \quad (64)$$

Using the Jacobi–Anger expansion [56], one finds

$$e^{i\phi_i(t)} = e^{i\varphi_i} \sum_{\ell \in \mathbb{Z}} J_\ell(\tilde{\beta}_i) e^{i(\ell \frac{\pi}{2} + \ell \Omega_{\text{rf}} t)}, \quad (65)$$

where $J_\ell(x)$ are the ℓ th order Bessel functions of the first class. This is the explicit expression for the Fourier series that was mentioned above equation (59), and leads to a clear picture for the appearance of the micromotion sidebands at frequencies $\ell \Omega_{\text{rf}}$. Depending on the particular value of the laser detuning $\delta \approx \ell_* \Omega_{\text{rf}}$, it is possible to address a particular micromotion sideband (59). Moreover, around each of these micromotion sidebands, there is an additional comb of frequencies representing the secular sidebands that occur at multiples of the secular normal-mode frequencies (48). By combining a pair of first secular sidebands, the spin-phonon couplings of equation (62) yield the desired state-dependent force.

3.2.1. Secular state-dependent dipole forces

The usual approach to obtain a state-dependent force relies on addressing the secular sidebands, $\delta \sim \omega_\alpha \ll \Omega_{\text{rf}}$ [28, 29–32], such that $\ell_* = 0$ according to our previous notation (59). By imposing the condition to resolve the micromotion sidebands

$$|\Omega_i^\alpha| \ll \Omega_{\text{rf}}, \quad (66)$$

and using the expression in equation (65) for the effects of excess micromotion, and equation (47) for the effects of the intrinsic micromotion, we find that the secular sidebands (62) can be expressed as a Hamiltonian with a state-dependent force

$$H_s(t) \approx \sum_{i,m} \mathfrak{F}_{i,m}^r x_m^\alpha \mathfrak{s}_i a_{m,\alpha}^\dagger e^{i\omega_{m,\alpha} t} \cos \delta t + \text{h.c.}, \quad (67)$$

where we have introduced a dipole-force strength

$$\mathfrak{F}_{i,m}^r = \frac{\Omega_i^\alpha \mathcal{M}_{i,m}^\alpha k_L}{\left(1 - \frac{q_\alpha}{2}\right)} \sqrt{J_0^2(\tilde{\beta}_i) + \left(\frac{q_\alpha}{4} J_1(\tilde{\beta}_i)\right)^2}, \quad (68)$$

and the following spin operator

$$\mathfrak{s}_i = \frac{1}{\sqrt{J_0^2(\tilde{\beta}_i) + \frac{q_\alpha^2}{16} J_1^2(\tilde{\beta}_i)}} \left(J_0(\tilde{\beta}_i) \tilde{\sigma}_i^y + \frac{q_\alpha}{4} J_1(\tilde{\beta}_i) \tilde{\sigma}_i^x \right). \quad (69)$$

Here, we have defined the Pauli matrices in a rotated basis with respect to the z -axis

$$\tilde{\sigma}_i^x := e^{i\frac{\varphi_i}{2}\sigma_i^z}(\sigma_i^+ + \sigma_i^-)e^{-i\frac{\varphi_i}{2}\sigma_i^z}, \quad \tilde{\sigma}_i^y := e^{i\frac{\varphi_i}{2}\sigma_i^z}(i\sigma_i^- - i\sigma_i^+)e^{-i\frac{\varphi_i}{2}\sigma_i^z}. \quad (70)$$

Accordingly, the spin operator (69) shares certain algebraic properties with the rotated Pauli matrices in equation (70), namely $\tilde{\mathfrak{s}}_i = \tilde{\mathfrak{s}}_i^\dagger$, $\tilde{\mathfrak{s}}_i^2 = \mathbb{I}$, and $[\tilde{\mathfrak{s}}_i, \tilde{\mathfrak{s}}_j] = 0$, which allow us to interpret equation (67) as a state-dependent force that pushes the vibrational modes in opposite directions depending on the two eigenstates of the spin operator $\tilde{\mathfrak{s}}_i = |+\tilde{\mathfrak{s}}_i\rangle\langle+\tilde{\mathfrak{s}}_i| - |-\tilde{\mathfrak{s}}_i\rangle\langle-\tilde{\mathfrak{s}}_i|$. In the limit of vanishing excess micromotion $\beta_i = 0$ (64), the phase $\varphi_i \approx \phi + k_L z_i^0 \delta_{\alpha,z}$, and equation (67) yields the aforementioned σ^ϕ -force of the Mølmer–Sørensen (MS) scheme [28] used in several experiments [29–32], where $\sigma^\phi = ie^{i\phi}\sigma^+ - ie^{-i\phi}\sigma^-$.

Let us note that, in addition to the desired state-dependent force (67), one has to consider the carrier terms (61), which in this regime (66) can be expressed as

$$H_c(t) = \sum_i \Omega_i^\alpha J_0(\tilde{\beta}_i) \tilde{\sigma}_i^x \cos \delta t. \quad (71)$$

This residual carrier does not commute with the dipole force (67), since the rotated Pauli matrices share the same $\mathfrak{su}(2)$ algebra as the original Pauli matrices. Therefore, the carrier and the dipole force will interfere and compromise the simple picture of the normal modes being displaced in opposite directions depending on the spin state. To minimize this undesired effect, the residual carrier must be far off-resonant, which can be achieved by limiting the laser intensity such that

$$|\Omega_i^\alpha J_0(\tilde{\beta}_i)| \ll \delta \sim \omega_\alpha, \quad (72)$$

and $H_c(t) \approx 0$ in a rotating-wave approximation. For vanishingly small micromotion $\tilde{\beta}_i \rightarrow 0$, this constraint (72) reduces to the standard condition required to work in the resolved-sideband regime $|\Omega_i^\alpha| \ll \omega_\alpha$. As a consequence, resolving the secular sidebands limits the intensity of the state-dependent force (68) that becomes in this regime

$$\tilde{\mathfrak{F}}_{i,m}^r = \Omega_i^\alpha \mathcal{M}_{i,m}^\alpha k_L \frac{1}{\left(1 - \frac{q_\alpha}{2}\right)}, \quad \tilde{\mathfrak{s}}_i \approx \tilde{\sigma}_i^y. \quad (73)$$

As discussed in the following section, it puts a constraint on the speed of entangling gates based on σ^ϕ -forces. Hence, it would be desirable to come up with schemes that yield similar state-dependent forces with milder constraints on their strengths. We now argue that this is possible by exploiting the higher micromotion sidebands.

3.2.2. Micromotion state-dependent dipole forces

Let us now discuss how to obtain a state-dependent force by addressing the first micromotion sideband, $\delta = \Omega_{\text{rf}} + \tilde{\delta}$, where $\tilde{\delta} \sim \omega_\alpha \ll \Omega_{\text{rf}}$, such that $\ell_* = 1$ according to our previous notation (59). Following an analogous derivation to the one above, we find the following Hamiltonian with a state-dependent force

$$H_s(t) \approx \sum_{i,m} \tilde{\mathfrak{F}}_{i,m}^r x_m^\alpha \tilde{\mathfrak{s}}_i a_{m,\alpha}^\dagger e^{i\omega_m t} \cos \tilde{\delta} t + \text{h.c.}, \quad (74)$$

where we have introduced a dipole-force strength

$$\tilde{\mathfrak{F}}_{i,m}^r = \frac{\Omega_i^\alpha \mathcal{M}_{i,m}^\alpha k_L}{\left(1 - \frac{q_\alpha}{2}\right)} \sqrt{J_1^2(\tilde{\beta}_i) + \left(\frac{q_\alpha}{4} J_0(\tilde{\beta}_i)\right)^2}, \quad (75)$$

and the following spin operator

$$\tilde{\mathfrak{s}}_i = \frac{1}{\sqrt{J_1^2(\tilde{\beta}_i) + \frac{q_\alpha^2}{16} J_0^2(\tilde{\beta}_i)}} \left(-J_1(\tilde{\beta}_i) \tilde{\sigma}_i^x + \frac{q_\alpha}{4} J_0(\tilde{\beta}_i) \tilde{\sigma}_i^y \right). \quad (76)$$

In analogy with the secular forces (67), we can interpret equation (74) as a state-dependent force that pushes the vibrational modes in opposite directions depending on the two eigenstates of the spin operator $\tilde{\mathfrak{s}}_i = |+\tilde{\mathfrak{s}}_i\rangle\langle+\tilde{\mathfrak{s}}_i| - |-\tilde{\mathfrak{s}}_i\rangle\langle-\tilde{\mathfrak{s}}_i|$.

The additional carrier term in equation (61) can be expressed in this case as

$$H_c(t) \approx \sum_i (\Omega_i^\alpha J_0(\tilde{\beta}_i) \tilde{\sigma}_i^x \cos \Omega_{\text{rf}} t - \Omega_i^\alpha J_1(\tilde{\beta}_i) \tilde{\sigma}_i^y \cos \tilde{\delta} t). \quad (77)$$

In principle, this term can cause a similar interference with the state-dependent force (74), since it does not commute with the spin operator in general (76). However, if the excess micromotion is minimized to the level

$$\tilde{\beta}_i \ll \frac{1}{4} q_\alpha \ll 1, \quad (78)$$

one gets $J_0(\tilde{\beta}_i) \approx 1$ and $J_i(\tilde{\beta}_i) \approx \tilde{\beta}_i$, such that the previous condition (72) to neglect the off-resonant carrier becomes less stringent. We find that the laser intensity will be limited by

$$|\Omega_i^\alpha| \ll \Omega_{\text{rf}}, \quad |\Omega_i^\alpha| \tilde{\beta}_i \ll \tilde{\delta} \sim \omega_\alpha, \quad (79)$$

and can be thus tuned to larger values in comparison to the secular scheme (72), where $|\Omega_i^\alpha| \ll \omega_\alpha$. According to this discussion, the advantage of the micromotion-enabled scheme in minimizing the undesired effects brought up by the off-resonant carrier with respect to the standard secular scheme will be larger the smaller $\omega_\alpha/\Omega_{\text{rf}}$ and $\tilde{\beta}_i$ can be made in the experiment. This will depend on the particular trap architecture, and the excess micromotion compensation capabilities discussed below. Let us finally note that the state-dependent force (75) becomes in this regime

$$\tilde{\mathfrak{F}}_{i,m}^r \approx \Omega_i^\alpha \mathcal{M}_{i,m}^\alpha k_L \frac{q_\alpha}{4(1 - \frac{q_\alpha}{2})}, \quad \tilde{\mathfrak{s}}_i \approx \tilde{\sigma}_i^y. \quad (80)$$

Comparing the strength of the secular (73) and micromotion (80) forces, one can see that to obtain similar strengths one would need to increase the Rabi frequency in the micromotion-scheme, and thus the laser power, by a factor of roughly $4/q_\alpha$. At this point, it is worth noting that we could have tuned the laser frequencies to a higher micromotion sideband $\delta = \Omega_{\text{rf}} + \ell_* \tilde{\delta}$ with $\ell_* > 1$. By doing this, the effect of the off-resonant carrier would be further suppressed $|\Omega_i^\alpha| \ll \ell_* \Omega_{\text{rf}}$. On the other hand, we would need even higher laser powers, increased by a factor of $4^{\ell_*} ((\ell_* - 1)!)^2 / (q_\alpha)^{\ell_*}$, to achieve forces of the same strength. Even if these laser intensities can be achieved in the laboratory, in this regime the intensity fluctuations could become a limiting factor for the gate performance. Accordingly, we will focus on the first micromotion sideband in the rest of this work.

3.3. Entanglement via geometric phase gates

We now discuss how to exploit the longitudinal/transverse phonons to mediate a qubit–qubit interaction capable of generating entanglement in the presence of micromotion. In order to have a simple description, we make use of the Magnus expansion [57], which allows us to express the time-evolution operator in the interaction picture as follows

$$U_I(t) = \mathcal{T} \left\{ e^{-i \int_0^t dt' H_I(t')} \right\} = e^{\mathcal{A}(t)}. \quad (81)$$

Here, the anti-Hermitian operator $\mathcal{A}(t) = -\mathcal{A}^\dagger(t)$ can be expressed as a series of time integrals over nested commutators

$$\mathcal{A}(t) = -i \int_0^t dt_1 H_I(t_1) - \frac{1}{2} \int_0^t dt_1 \int_0^{t_1} dt_2 [H_I(t_1), H_I(t_2)] + \dots, \quad (82)$$

which can be truncated to the desired order of approximation. This will allow us to discuss the generation of entanglement through a generic Hamiltonian with a state-dependent force $H_I(t) = H_s(t)$, which encompasses both equation (67) and equation (74), and allows for an additional pulse shaping on the forces $\tilde{\mathfrak{F}}_{i,m}^r \rightarrow \tilde{\mathfrak{F}}_{i,m}^r(t)$.

In this ideal situation, the Magnus expansion (82) becomes exact already at second order, such that

$$\mathcal{A}(t) = \sum_{i,m} \mathfrak{s}_i (\gamma_{i,m}(t) a_{m,\alpha} - \gamma_{i,m}^*(t) a_{m,\alpha}^\dagger) + \sum_{i,j} g_{ij}(t) \mathfrak{s}_i \mathfrak{s}_j, \quad (83)$$

where we have introduced the following parameters

$$\gamma_{i,m}(t) = -i \int_0^t dt_1 \tilde{\mathfrak{F}}_{i,m}^r(t_1) x_m^\alpha \cos(\delta t_1) e^{-i\omega_{m,\alpha} t_1}, \quad (84)$$

$$g_{ij}(t) = i \int_0^t dt_1 \int_0^{t_1} dt_2 \sum_m \tilde{\mathfrak{F}}_{i,m}^r(t_1) x_m^\alpha \tilde{\mathfrak{F}}_{j,m}^r(t_2) x_m^\alpha \cos(\delta t_1) \cos(\delta t_2) \sin(\omega_{m,\alpha} (t_1 - t_2)). \quad (85)$$

Hence, the Magnus expansion operator (83) amounts to a state-dependent displacement of the vibrational modes, followed by an effective spin–spin interaction that is capable of generating the desired entanglement between the trapped-ion qubits. On the contrary, the displacement will degrade the quality of the quantum logic gate, as it leads to residual entanglement between the qubits and the phonons, contributing with a motional error that must be minimized. If $\gamma_{i,m}(t_g) \approx 0$, the vibrational modes develop a closed trajectory in phase space, returning to the initial state after a particular gate time t_g . Along these closed trajectories, the qubits acquire a state-dependent geometric phase that depends on the enclosed phase-space area, and can be exploited to generate maximally entangled states [26, 28].

For instance, considering $N = 2$ and an initial state $\rho_0 = |\psi_0\rangle\langle\psi_0| \otimes \rho_{\text{th}}$, where $|\psi_0\rangle = |\downarrow_1 \downarrow_2\rangle$ is the state of two qubits after optical pumping, and ρ_{th} is the state of the vibrational modes after laser cooling, the time-evolved state under a secular state-dependent force (67) in the limit of $\beta_i \ll 1$ becomes $\rho(t_g) = |\psi(t_g)\rangle\langle\psi(t_g)| \otimes \rho_{\text{th}}$, where

$$|\psi(t_g)\rangle = \frac{1}{\sqrt{2}}|\downarrow_1\downarrow_2\rangle + \frac{i}{\sqrt{2}}e^{i(\varphi_1+\varphi_2)}|\uparrow_1\uparrow_2\rangle \quad (86)$$

is locally equivalent to a Bell state, and we have assumed that the laser intensities have values such that $2g_{12}(t_g) = -i\pi/4$.

In the following subsections, we will consider different possibilities of achieving $\gamma_{i,m}(t_g) \approx 0$, and $g_{ij}(t_g) = -i\pi/8$ for a crystal of two trapped ions. We start by reviewing the entangling gates that use continuous-wave (CW) state-dependent forces in the secular regime (67). We first describe gate schemes that exploit a single vibrational mode (i.e. bus mode) to mediate the entanglement between the qubits [28, 29–32], and discuss the limitations in gate speed arising from the necessity to resolve single vibrational modes. We then consider schemes that address both vibrational modes using a CW secular force, and discuss the limitations on the speed imposed by the minimization of spin-motion entanglement of both bus modes. Finally, we move onto a discussion of pulsed schemes, which can overcome both limitations on the gate speed, but will be limited by the restriction on the Rabi frequencies (72) to neglect the additional off-resonant carrier. This long discussion will allow us to embark upon the description of entangling gates using the micromotion state-dependent-forces of section 3.2.2, assuming that equation (78) is fulfilled, and discussing the improvement on the gates that this scheme can lead to.

3.3.1. Entangling gates with secular forces

Let us particularize the Magnus operator (83) to the secular state-dependent dipole force (67), which we will assume to be composed of a sequence of N_p square pulses

$$\mathfrak{F}_{i,m}^r(t) = \sum_{n_p=1}^{N_p} f_{i,m}^{n_p}(\theta(t - t_{n_p}) - \theta(t - (t_{n_p} + \tau_{n_p}))). \quad (87)$$

Here, $f_{i,m}^{n_p}$ is the force of the n_p th pulse obtained from equation (68) by substituting the Rabi frequency Ω_{i,n_p}^α of that particular pulse, and $\theta(x)$ is the Heaviside step function, such that this pulse acts within a time window $t \in [t_{n_p}, t_{n_p} + \tau_{n_p})$. In order to use the above generic Magnus expansion, the additional off-resonant carrier (77) must be negligible, which requires the laser parameters to lie in the regime (72). Moreover, we will focus on the regime where the excess micromotion is very-well compensated, such that equation (72) leads to $|\Omega_i| \ll \omega_\alpha$, and thus $|f_{i,m}^{n_p} x_m| \ll (\delta + \omega_m)$ follows from equation (68). This constraint over the forces allows us to simplify considerably the particular expressions for the parameters (84) and (85) for single- and multi-pulse gates.

(i) *Single-pulse entangling gates:* Let us consider equation (87) for a single pulse $n_p = N_p = 1$ of strength $f_{i,m}$, between $t_{n_p} = 0$ and $\tau_{n_p} = t_g$ [28, 29–32]. By performing the corresponding integrals, one finds the state-dependent displacements

$$\gamma_{i,m}(t_g) \approx \frac{f_{i,m} x_m^\alpha}{2} \frac{1 - e^{i(\delta - \omega_{m,\alpha})t_g}}{\delta - \omega_{m,\alpha}}, \quad (88)$$

and the phonon-mediated spin–spin interactions

$$g_{12}(t_g) = i \sum_m \frac{f_{1,m} x_m^\alpha f_{2,m} x_m^\alpha}{2(\omega_{m,\alpha}^2 - \delta^2)} \left(\omega_{m,\alpha} t_g + \frac{\omega_{m,\alpha} \sin(\delta - \omega_m)t_g}{\delta - \omega_{m,\alpha}} \right). \quad (89)$$

(a) *Addressing a single vibrational mode.* Let us start by considering single-pulse gates that resolve a single bus mode to mediate the interaction, such as the center-of-mass (CoM) mode $\delta \approx \omega_{1,\alpha}$ of either longitudinal or transverse vibrations. The condition to resolve a single vibrational mode for a $N = 2$ ion crystal is

$$|f_{i,m} x_m^\alpha| \ll |\omega_{1,\alpha} - \omega_{2,\alpha}|, \quad (90)$$

such that $\gamma_{i,2}(t_g) \approx 0$ for the remaining vibrational mode, which only acts as a spectator mode. Hence, one only needs to set the gate time t_g such that $\gamma_{i,1}(t_g) = 0$ in order to minimize the residual spin-motion entanglement of the bus mode. This is accomplished by setting the following relation between laser detuning and the gate time

$$t_g = 2\pi \frac{r_1}{|\delta - \omega_{1,\alpha}|}, \quad (91)$$

where $r_1 \in \mathbb{Z}^+$ [28]. The phase-space trajectory defined by $\gamma_{i,1}(t_g) = 0$, and induced by the displacement operator (83), corresponds to r_1 closed circular loops, such that spin and motional degrees of freedom get disentangled at the end of the gate. Conversely, the two spins can get maximally entangled. Using $2g_{12}(t_g) \approx -it_g J_{12}$, one finds that the time-evolution operator (81)–(83) can be expressed as

$$U_1(t_g) = e^{-it_g J_{12} s_1 s_2}, \quad (92)$$

where we have introduced the spin–spin coupling strengths

$$J_{12} = \omega_R \Omega_1^\alpha \Omega_2^\alpha \frac{J_0(\beta_1) J_0(\beta_2)}{\left(1 - \frac{1}{2} q_\alpha\right)^2} \sum_m \frac{\mathcal{M}_{1,m}^\alpha \mathcal{M}_{2,m}^\alpha}{\delta^2 - \omega_{m,\alpha}^2}, \quad (93)$$

where $\omega_R = k_L^2/2M$ is the recoil energy. Considering a negligible excess micromotion $\beta_i \ll 1$, the coupling becomes $J_{12} \approx (\Omega^\alpha \eta_1^\alpha)^2 \omega_{1,\alpha} / 2(\delta^2 - \omega_{1,\alpha}^2) \approx (\Omega^\alpha \eta_1^\alpha)^2 / 4(\delta - \omega_{1,\alpha})$ to leading order of the Lamb–Dicke parameter. This coincides with the expression in [28] up to a different definition of their Lamb–Dicke parameter that incorporates the normal-mode displacements.

The condition to generate a maximally entangled state using equation (92) is $J_{12} t_g = \pi/4$, which sets another constraint between laser detuning and the gate time

$$\frac{(\Omega^\alpha \eta_1^\alpha)^2}{|\delta - \omega_{1,\alpha}|} t_g = \pi. \quad (94)$$

Solving the system of algebraic equations (91) and (94) fixes the detuning as a function of the number r_1 of closed loops in phase space, and the Rabi frequency of the transition Ω^α . Accordingly, the gate time can be shown to be

$$t_g = \frac{\pi}{\Omega^\alpha \eta_1^\alpha} \sqrt{2r_1}, \quad (95)$$

such that the stronger the intensity of the laser is, the larger Ω^α becomes, and the faster the entangling gate is, e.g. $t_g = \sqrt{2} \pi / \Omega^\alpha \eta_1^\alpha$ for gates based on 1-loop trajectories. We note that this intensity increase must be accompanied by a corresponding increase in the detuning of the laser beams

$$\delta = \omega_\alpha + \sqrt{2r_1} \Omega^\alpha \eta_1^\alpha. \quad (96)$$

However, such an increase in gate speed cannot be prolonged indefinitely. Let us recall that the condition to resolve a single vibrational mode (90) puts a constraint on the laser intensity $\Omega \eta_1^\alpha \ll |\omega_{1,\alpha} - \omega_{2,\alpha}|$, such that the gate speed is limited by

$$t_g \gg \frac{\pi}{|\omega_{1,\alpha} - \omega_{2,\alpha}|}. \quad (97)$$

This gate-speed limitation is very different for MS gates that use longitudinal or transverse phonons as the quantum bus to mediate the qubit–qubit entanglement.

(a.1) *For longitudinal phonons*, the modes fulfill $|\omega_{1,z} - \omega_{2,z}| \sim \omega_z$, such that the gate speed is ultimately limited by the trap period $t_g \gg 2\pi/\omega_z$. Let us emphasize, however, that the gate fidelity would decrease for such fast gates, which sets a lower speed limit in practice. Maximizing the gate speed by increasing the Rabi frequency within the valid parameter regime (90), namely $\Omega^z \ll |\omega_{1,z} - \omega_{2,z}|/\eta_1^z \sim \omega_z/\eta_1^z$, can lead to situations where the contribution of the off-resonant carrier (77) is not negligible anymore, i.e. $\Omega^z \ll \omega_z$ in equation (72) begins to be violated. Accordingly, if the gate speed increases beyond a certain limit, the off-resonant carrier will increase the gate error and dominate over other sources of noise.

To quantify this effect, we estimate the state infidelity $\epsilon_g = 1 - \mathcal{F}_g$ for the generation of the desired Bell state (86) as a function of the gate time. We consider three different sources of infidelity $\epsilon_g = \epsilon_{\text{carr}} + \epsilon_{\text{mot}} + \epsilon_{\text{deph}}$: the off-resonant carrier (77) leads to $\epsilon_{\text{carr}} \approx \frac{1}{2} N (\Omega^z/\delta)^2$ [28]⁵, the additional terms neglected in the Lamb–Dicke expansion (57), including the effect of spectator modes, lead to a motional error $\epsilon_{\text{mot}} \approx 0.8\pi N (\delta - \omega_z)(\bar{n}_z + 1)/(2\omega_z^2 t_g) + \pi^2 N (N - 1)(\eta_1^z)^4 (1.2\bar{n}_z^2 + 1.4\bar{n}_z)/8N^2$ [28], where we have assumed a thermal state for the longitudinal vibrational modes, such that \bar{n}_z is the mean number of phonons in the thermal CoM mode. Finally, we also consider dephasing during the gate, which can be caused by fluctuating global magnetic fields, which lead to $\epsilon_{\text{deph}} \approx 2N^2 t_g/T_2$, where T_2 is the dephasing time of the qubits, as measured by Ramsey interferometry. In figure 1, we represent the full error as a function of the gate time for different dephasing rates, choosing ⁴⁰Ca⁺ qubits as a representative case [58]. This figure demonstrates that for cold crystals with $\bar{n}_z = 0.1$, the motional error of MS gates is negligible in comparison to the errors due to the dephasing and the off-resonant carrier. This would occur also for warmer crystals with the same parameters, provided that $\bar{n}_z \leq 5$, after which the motional-error contribution cannot be neglected any longer. Whereas for slow gates, the ϵ_{deph} contribution is dominant, ϵ_{carr} becomes the leading source of infidelity when the gate becomes sufficiently fast. As predicted above, the gate is always slower than the trap period $T_t = 2\pi/\omega_z = 1\mu\text{s}$ if one aims for reasonably high fidelities $\epsilon_g < 10^{-2}$. In section 3.3.2, we will discuss how it is possible to increase the gate speed further, while maintaining high fidelities, provided that the intrinsic axial micromotion of the ion crystal can be exploited to shape the micromotion state-dependent forces (74) instead of the secular ones (67).

⁵ This particular expression for the contribution of the off-resonant carrier to the error budget is an upper bound derived in [28]. We note that even if the carrier error is smaller than this value, the general trend discussed in this work will remain, i.e. it will become the leading error for sufficiently fast gates.

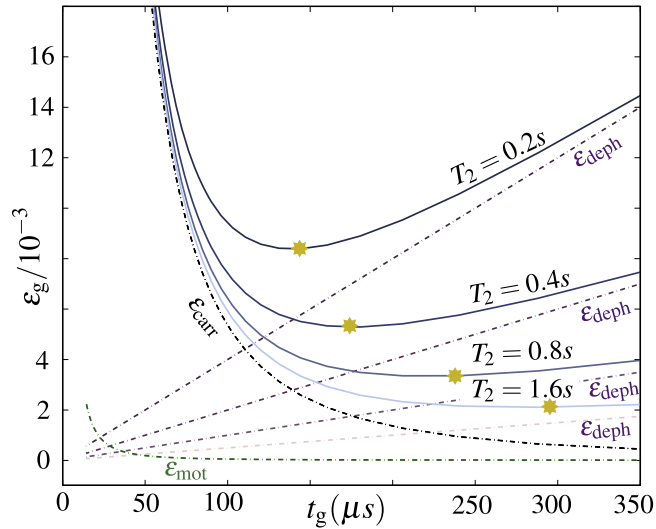


Figure 1. Single-pulse MS gate with the axial CoM mode: State infidelity ϵ_g for a MS gate mediated by the CoM longitudinal mode of a $N = 2$ crystal of $^{40}\text{Ca}^+$ ions. We assume an axial trap frequency $\omega_z/2\pi = 0.975$ MHz, such that the single-ion Lamb–Dicke parameter is $\eta_1^z = 0.098$, resolved-sideband laser-cooling leading to $\bar{n}_z = 0.1$ for the CoM mode, and set the number of phase-space loops of the MS gate to $r_1 = 1$. The blue solid lines correspond to the total state infidelity ϵ_g for dephasing times $T_2 \in \{0.2, 0.4, 0.8, 1.6\}$ s, whereas the dotted lines represent the contributions of dephasing, motional, and carrier errors, as indicated in the captions. The yellow stars represent the optimum gate times with respect to the highest-possible gate fidelity for each set of parameters. To vary the gate speed, we consider increasing the Rabi frequency within $\Omega^2/2\pi \in [0.02, 0.12]$ MHz, and setting the corresponding detunings $(\delta - \omega_z)/2\pi \in [2.9, 16.6]$ kHz according to the equations discussed in the text.

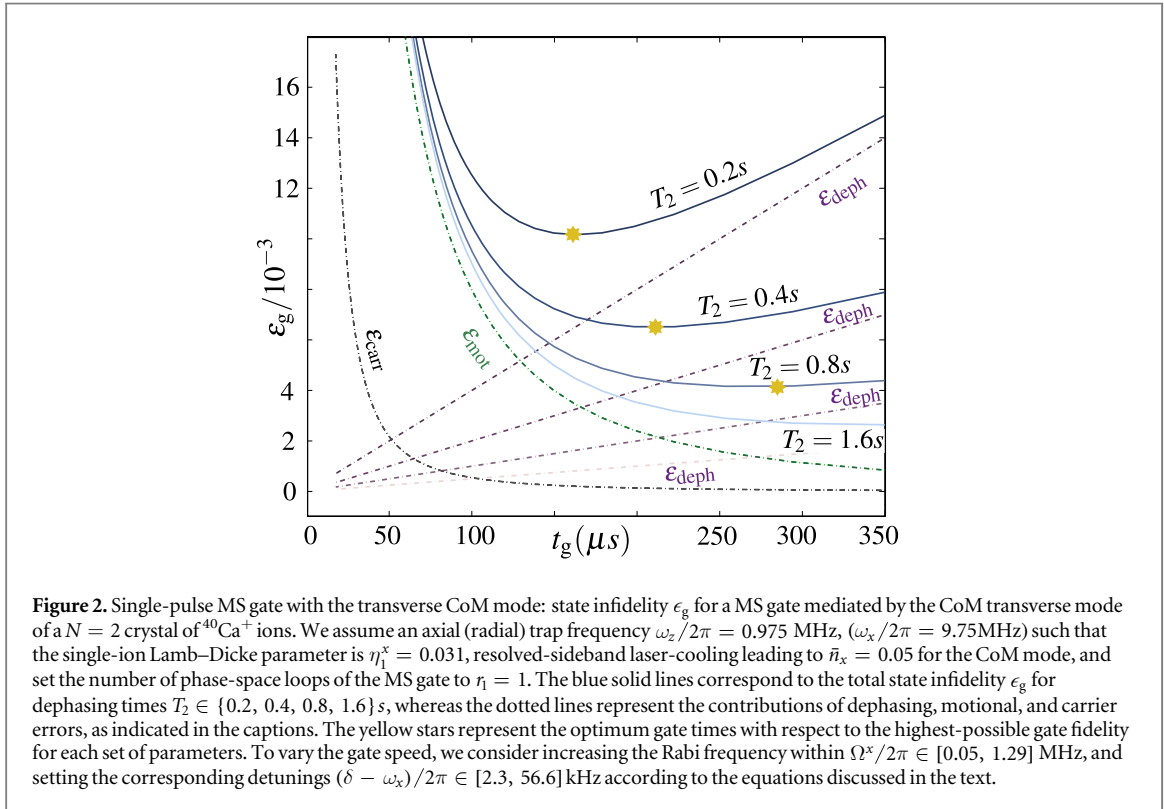
(a.2) For transverse phonons, the situation can first appear favorable, since the trap frequencies are larger, and one can naively expect that $\delta \sim \omega_x$ can be achieved with larger detunings, and thus shorter gate times (91). However, the condition to resolve a single mode (90) is more stringent, since $|\omega_{1,x} - \omega_{2,x}| \sim (\omega_z/\omega_x)^2 \omega_x \ll \omega_z$ for the usual regime of linear Paul traps $\omega_z \ll \omega_x$. Therefore, exploiting the available larger detunings to speed up the gate leads inevitably to a decrease in fidelity. We note that the condition to resolve a single mode imposes $\Omega^x \ll |\omega_{1,x} - \omega_{2,x}|/\eta_1^x \ll \omega_z/\eta_1^x \ll \omega_x/\eta_{1,x}^x$. Hence, even if the gate speed is maximized, one would not reach the regime where the off-resonant carrier starts to be problematic since $\Omega^x \ll \omega_x$ is always warranted. Hence, the error for fast MS gates will be dominated by the contribution to the motional error of the spectator modes.

To quantify this discussion, we estimate again the state infidelity $\epsilon_g = 1 - \mathcal{F}_g$ for generating the desired Bell state (86) as a function of the gate time. The carrier and dephasing errors have the same expressions as above, whereas the motional error changes due to the proximity of the spectator modes in frequency space. For $N = 2$, we get $\epsilon_{\text{mot}} \approx (\Omega^x \eta_2^x)^2 (2\bar{n}_x + 1) (\delta^2 + \omega_{2,x}^2) / (\delta^2 - \omega_{2,x}^2)^2$, where we have assumed a thermal state for the transverse vibrational modes with mean phonon number \bar{n}_x . In figure 2, we represent the full error as a function of the gate time for different dephasing rates, choosing $^{40}\text{Ca}^+$ qubits to compare with the previous longitudinal gate. As announced earlier, this figure shows that the error of slow (fast) gates is dominated by the dephasing (motional) error. One also observes, that the optimum transverse gates are always slower than the longitudinal ones in figure 1 and, moreover, achieve smaller fidelities.

Let us also note that both of these longitudinal and transverse entangling gates can be generalized to N -qubits, and would lead to multi-partite maximal entangled states locally equivalent to $|\text{GHZ}\rangle_N = (|\downarrow_1 \downarrow_2 \cdots \downarrow_N\rangle + |\uparrow_1 \uparrow_2 \cdots \uparrow_N\rangle) / \sqrt{2}$, instead of the Bell state (86). The conditions to generate such states using MS gates based on the longitudinal CoM mode remain the same, since such a bus mode is always separated from higher-frequency modes by the same frequency gap [53]. On the contrary, the conditions on MS gates based on the transverse CoM mode lead to even slower gates, since the phonon branch becomes denser, and the different modes approach the CoM frequency as N increases.

(b) Addressing both vibrational modes. Let us now address how to increase the gate speed by lifting the constraint (90), such that the state-dependent force does not resolve a single vibrational mode even when $\delta \approx \omega_{1,\alpha}$. For $N = 2$ ions, two conditions are required to minimize the spin-motion entanglement, namely $\gamma_{i,1}(t_g) = 0$, and $\gamma_{i,2}(t_g) = 0$. The first one sets the relation in equation (91) between the gate time and the detuning, whereas the yields a commensurability condition

$$\delta - \omega_{2,\alpha} = r_2(\delta - \omega_{1,\alpha}), \quad (98)$$



where $r_2 \in \mathbb{Z}$, which already fixes the detuning to

$$\delta = (r_2\omega_{1,\alpha} - \omega_{2,\alpha})/(r_2 - 1). \quad (99)$$

(b.1) For longitudinal modes, the condition (98) cannot be met, as the frequency difference is an irrational number $\omega_{2,z} - \omega_{1,z} = (\sqrt{3} - 1)\omega_z$. In any case, the gate-speed could not be increased even if one could close both trajectories perfectly, as the limitation on gate speed is given by the condition to neglect the off-resonant carrier (see figure 1). Equivalently, this would not improve the gate fidelity of the MS gates too much, as the motional error due to the spectator vibrational mode is already very small for typical experimental values (see figure 1).

(b.2) For transverse modes, in contrast, the condition (98) can be met and the allowed gate times correspond to trajectories with r_1 loops for the CoM mode $\omega_{1,x}$, and $r_1|r_2|$ for the zigzag mode $\omega_{2,x}$ with $r_2 \geq 2$ or $r_2 \leq -1$. These two conditions suffice to fix the gate time to

$$t_g = 2\pi \frac{r_1|r_2 - 1|}{(\omega_{1,x} - \omega_{2,x})}. \quad (100)$$

The remaining task is to find the required laser intensity such that the state-dependent geometric phase proportional to the enclosed phase-space area fulfills the condition to generate a maximally entangled state $J_{12}t_g = \pi/4$. In this case, one has to consider the contribution of both modes to the spin–spin coupling strength (93), which becomes $J_{12} \approx (\Omega^x\eta_1^x)^2(1/4(\delta - \omega_{1,x}) - 1/4(\delta - \omega_{2,x}))$. Using the expression for the fixed detuning (99), one finds that the required laser Rabi frequency is

$$\Omega^x\eta_1^x = \frac{(\omega_{1,x} - \omega_{2,x})}{|r_2 - 1|} \sqrt{\frac{|r_2|}{2r_1|r_2 - 1|}}. \quad (101)$$

As occurred for the MS gates that use a single vibrational bus mode (95), the gate can become faster by increasing the laser Rabi frequency, since the expression

$$t_g = \frac{\pi}{\Omega^x\eta_1^x} \sqrt{\frac{2|r_2|}{r_1|r_2 - 1|^3}}, \quad (102)$$

yields $t_g = 2\pi/\Omega^x\eta_1^x$ for the fastest gate with $r_2 = 2r_1 = 2$ loops. Let us note that this gate time can also be expressed as

$$t_g = \frac{2\pi}{\omega_{1,x} - \omega_{2,x}}, \quad (103)$$

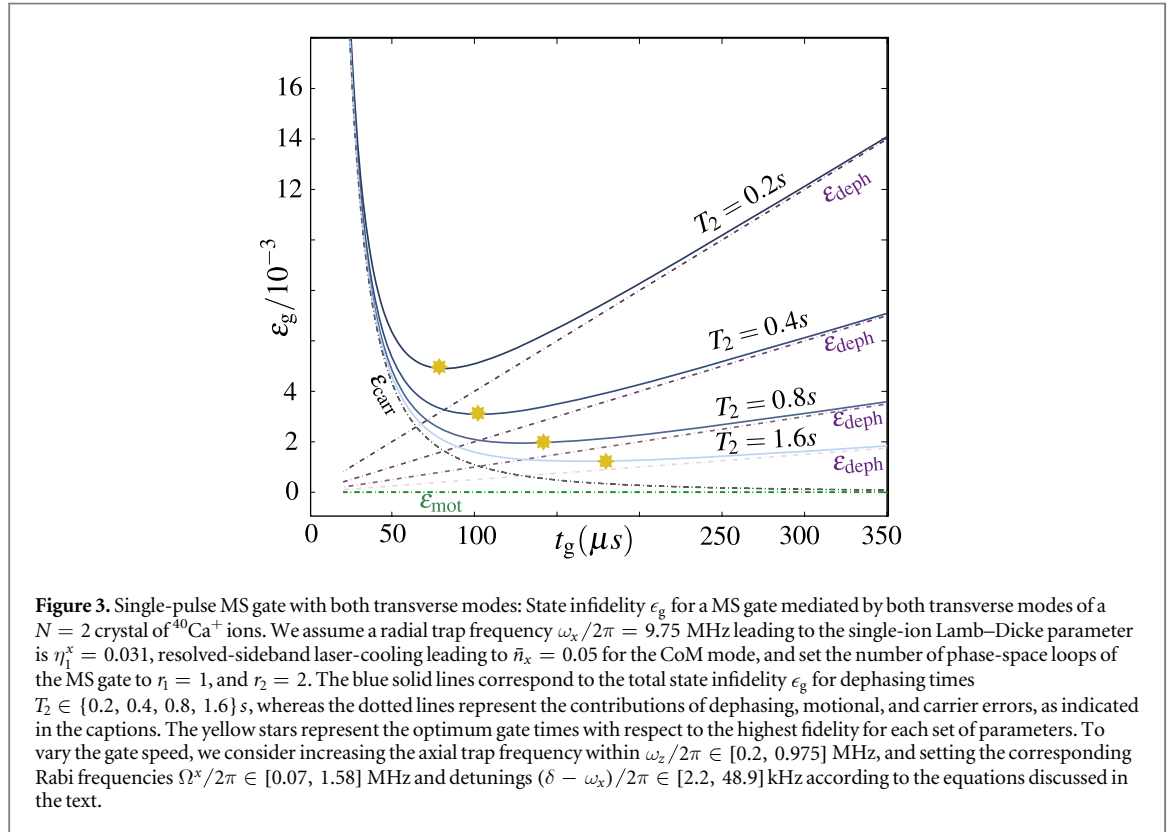


Figure 3. Single-pulse MS gate with both transverse modes: State infidelity ϵ_g for a MS gate mediated by both transverse modes of a $N = 2$ crystal of $^{40}\text{Ca}^+$ ions. We assume a radial trap frequency $\omega_x/2\pi = 9.75$ MHz leading to the single-ion Lamb–Dicke parameter is $\eta_1^x = 0.031$, resolved-sideband laser-cooling leading to $\bar{n}_x = 0.05$ for the CoM mode, and set the number of phase-space loops of the MS gate to $r_1 = 1$, and $r_2 = 2$. The blue solid lines correspond to the total state infidelity ϵ_g for dephasing times $T_2 \in \{0.2, 0.4, 0.8, 1.6\}$ s, whereas the dotted lines represent the contributions of dephasing, motional, and carrier errors, as indicated in the captions. The yellow stars represent the optimum gate times with respect to the highest fidelity for each set of parameters. To vary the gate speed, we consider increasing the axial trap frequency within $\omega_z/2\pi \in [0.2, 0.975]$ MHz, and setting the corresponding Rabi frequencies $\Omega^x/2\pi \in [0.07, 1.58]$ MHz and detunings $(\delta - \omega_x)/2\pi \in [2.2, 48.9]$ kHz according to the equations discussed in the text.

which shows that by exploiting both vibrational modes simultaneously, the speed can be increased with respect to the limitation of the previous transverse MS gates (97).

We note that the procedure of increasing the gate speed is slightly more involved than that of single-mode MS gates (95), which only required increasing simultaneously the Rabi frequency and the detuning of the laser beams (96). For two-mode MS gates, equation (101) shows that in addition one needs to increase the frequency difference between both vibrational modes, which requires modifying the trap confinement. In particular, we consider increasing the axial trap frequency ω_z , since $(\omega_{1,x} - \omega_{2,x}) \sim (\omega_z/\omega_x)^2 \omega_x$, and this will increase the gate speed (103). The ultimate limit to such an increase in gate speed is caused by the structural instability of the ion chain towards a zig-zag ladder, which occurs for $\omega_z \approx \omega_x$ for $N = 2$ ions. According to equation (103), this limit corresponds to a gate that could be as fast as the trap period $T_t = 2\pi/\omega_x$. However, note that the required Rabi frequency in this ultimate limit would largely violate the condition to neglect the off-resonant carrier (72), as $\Omega^x \sim (\omega_{1,x} - \omega_{2,x})/\eta_1^x \sim (\omega_z/\omega_x)^2 \omega_x/\eta_1^x \sim \omega_x/\eta_1^x \gg \omega_x$. Accordingly, this fast gate would have poor fidelities. Another effect that would decrease the gate fidelity even further is the increasing importance of nonlinear quartic terms in the vibrational Hamiltonian as one approaches the structural instability, which would modify the simple phase-space trajectories of the MS schemes.

Therefore, at a practical level, the limit on gate speed for high-fidelity MS gates based on two transverse bus modes would be to consider $\omega_z/\omega_x \sim \sqrt{\eta_1^x/10}$, such that $t_g \approx 2\pi/(\omega_z/\omega_x)^2 \omega_x \gg 2\pi/\omega_z \gg 2\pi/\omega_x$. Although this gate is still considerably slower than the trap period, there will be particular ratios ω_z/ω_x , such that the transverse MS gate may surpass the speed of the longitudinal one. In this sense, by resolving the two vibrational modes, the transverse MS gate can exploit the larger available detunings to achieve higher speeds, while maintaining high fidelities.

To quantify this discussion, we estimate again the state infidelity $\epsilon_g = 1 - \mathcal{F}_g$ for generating the desired Bell state (86) as a function of the gate time. The carrier and dephasing errors have the same expressions as above, whereas the motional error changes once more since both modes are active buses, and the leading order error will only be caused by the higher-order terms in the Lamb–Dicke expansion (57). For $N = 2$, we get $\epsilon_{\text{mot}} \approx 2 \times \pi^2 N(N-1)(\eta_1^x)^4(\bar{n}_x^2 + \bar{n}_x)/8N^2$, where we have assumed a thermal state for the transverse vibrational modes with mean phonon number \bar{n}_x . In figure 3, we represent the full error as a function of the gate time for different dephasing rates, choosing $^{40}\text{Ca}^+$ qubits to compare with the previous gates. As announced earlier, this figure shows that the error of fast gates is dominated by the off-resonant carrier error. We note that the optimum transverse gates shown in this figure are faster and more accurate than the longitudinal and transverse gates of figures 1 and 2. Regarding the comparison to the longitudinal-gate performance of figure 1, we note that the set of axial trap frequencies used in figure 2 is always below the axial trap frequency of figure 1

(see the particular values in both captions). Accordingly, the performance and speed shown in figure 1 sets an upper bound for the comparison of axial and transverse gates, and one concludes that the the transverse MS gate can indeed achieve higher speeds and fidelities. In section 3.3.2, we will discuss how to increase the gate speed even further, while achieving also higher fidelities, in traps where the intrinsic radial micromotion can be exploited.

(ii) *Multi-pulse entangling gates.* In the previous section, we have shown how to increase the speed of single-pulse MS gates by increasing the laser intensity. Let us now address an alternative strategy to speed up the entangling gates by considering a multi-pulse scheme with N_p pulses (87). In addition to increasing the laser intensity, one can also explore how to distribute it among the different pulses in order to attain higher speeds without compromising the gate fidelities.

To analyze this multi-pulse scheme, we need to find the particular expression for the time-evolution operator in equations (81) and (83). By performing the corresponding integrals in equations (84) and (85), we find the following state-dependent displacements and phonon-mediated interaction strengths

$$\gamma_{i,m}(t_g) = \Delta\gamma_{i,m}^{N_p}, \quad \Delta\gamma_{i,m}^{N_p} = \sum_{n'_p=1}^{n_p} \gamma_{i,m}^{n'_p}, \quad g_{12}(t_g) = -i\frac{J_{12}^{N_p}}{4}t_g + \delta g_{12} + \sum_m \sum_{n_p=1}^{N_p} \Delta\gamma_{2,m}^{n_p-1} (\gamma_{1,m}^{n_p})^* - \text{h.c.} \quad (104)$$

Here, we have introduced the following constants

$$\begin{aligned} \gamma_{i,m}^{n_p} &= \frac{f_{1,m}^{n_p} x_m^\alpha}{2} (C_{\delta-\omega_{m,\alpha}}^{\tau_{n_p}} e^{i(\delta-\omega_{m,\alpha})t_{n_p}} + C_{-\delta-\omega_{m,\alpha}}^{\tau_{n_p}} e^{-i(\delta+\omega_{m,\alpha})t_{n_p}}), \quad J_{12}^{n_p} = \sum_m \frac{f_{1,m}^{n_p} x_m^\alpha f_{2,m}^{n_p} x_m^\alpha \omega_{m,\alpha}}{\delta^2 - \omega_{m,\alpha}^2}, \\ \delta g_{12} &= \sum_m \sum_{n_p} \frac{f_{1,m}^{n_p} x_m^\alpha f_{2,m}^{n_p} x_m^\alpha}{8} \left(\frac{C_{-\delta+\omega_{m,\alpha}}^{\tau_{n_p}} + (C_{\delta+\omega_{m,\alpha}}^{\tau_{n_p}} - C_{2\delta}^{\tau_{n_p}}) e^{i2\delta t_{n_p}}}{-\delta + \omega_{m,\alpha}} + \frac{C_{\delta+\omega_{m,\alpha}}^{\tau_{n_p}} + (C_{-\delta+\omega_{m,\alpha}}^{\tau_{n_p}} - C_{-2\delta}^{\tau_{n_p}}) e^{-i2\delta t_{n_p}}}{\delta + \omega_{m,\alpha}} \right), \end{aligned} \quad (105)$$

and used the circle function, $C_\omega^\tau = (1 - e^{i\omega\tau})/\omega$ [38]. As a consistency check, note that for a single CW pulse $N_p = 1$, $t_{n_p} = 0$, the terms $f_{i,m}^{n_p} x_m^\alpha C_\omega^{\tau_{n_p}}$ with $\omega \approx \omega_\alpha$ can be neglected by a rotating-wave approximation for $|f_{i,m}^{n_p} x_m^\alpha| \ll (\delta + \omega_m)$, which follows from equation (72). Accordingly, one gets the simplified expressions in equations (88) and (89), which were the starting point in the analysis of the previous section.

To illustrate how the CW schemes can be modified to improve the gate speed, we focus on schemes of equidistant laser pulses of identical widths [59, 60]. In this case, one has $\tau_{n_p} = \tau := t_g/N_p$, and $t_{n_p} = \tau(n_p - 1)$ in equation (87). The conditions $\gamma_{i,m}(t_g) = 0$ yield a linear system of equations

$$\sum_{n_p} \text{Re} \{z_{m,n_p}\} \Omega_{i,n_p}^\alpha = 0, \quad \sum_{n_p} \text{Im} \{z_{m,n_p}\} \Omega_{i,n_p}^\alpha = 0, \quad (106)$$

where $z_{m,n_p} = C_{\delta-\omega_{m,\alpha}}^{\tau_{n_p}} e^{i(\delta-\omega_{m,\alpha})t_{n_p}} + C_{-\delta-\omega_{m,\alpha}}^{\tau_{n_p}} e^{-i(\delta+\omega_{m,\alpha})t_{n_p}}$, and we denote the Rabi frequencies for each of the pulses as Ω_{i,n_p}^α . Therefore, for N ions and thus N normal modes along a particular trap axis, one has a system of $2N$ linear equations, and a non-trivial solution of equation (106) can be found if we allow for $N_p = 2N + 1$ different pulses. This solution fixes the relative Rabi frequencies of the pulses $\{\Omega_{i,n_p}^\alpha / \Omega_{i,1}^\alpha\}_{n_p=2}^{N_p}$. Since we want to study the conditions that allow for a speed-up with respect to the single-pulse gates in equations (95) or (103), we shall fix the detuning to the corresponding optimal value, either equation (96) or equation (99) for single/two-mode schemes. Hence, the only remaining equation comes from the condition to generate a maximally entangled state $g_{ij}(t_g) = -i\pi/8$. This will suffice to fix $\Omega_{i,1}^\alpha$ for a particular gate time, such that we can target pulse sequences that yield faster gates.

(a) *Addressing a single vibrational mode.* Let us first address how to increase the speed of the single-pulse gates based on the longitudinal CoM mode (figure 1) by exploiting a train of equidistant pulses. For the longitudinal modes, the large frequency gap of the CoM mode with respect to other vibrational modes allows us to reduce the number of required pulses to $N_p = 3$. We follow the above method to find the optimal pulse sequence for a fixed detuning and a certain gate time. Starting from the gate time of the highest-fidelity MS gates (see the stars in figure 1), we lower the target gate time, and search for pulse sequences that close the CoM phase-space trajectory for a fixed detuning (96) that does no longer fulfill equation (91).

In order to assess quantitatively if the performance of the pulsed MS gate is also optimal, i.e. highest fidelity, we use again the error model underlying figure 1, as discussed in the previous section. However, for the error due to the off-resonant carrier, we consider $\epsilon_{\text{carr}} \approx \frac{1}{2}N \overline{(\Omega^z)^2} / \delta^2$ with $\overline{(\Omega^z)^2} = \sum_{n_p} (\Omega_{n_p}^z)^2 / N_p$, which takes into account the distribution of the Rabi frequencies within the pulse train. The results are presented in figure 4, which shows that one can obtain an additional speed-up by using a pulse train with state-dependent forces that alternate their direction. Moreover, the intermediate pulse is very weak, which allows one to reduce the required average Rabi frequency with respect to the single-pulse gates, and leads to a lower gate infidelity. If the multi-pulsed gate speed is increased above this optimum point, the infidelity rises quickly due to the contribution of

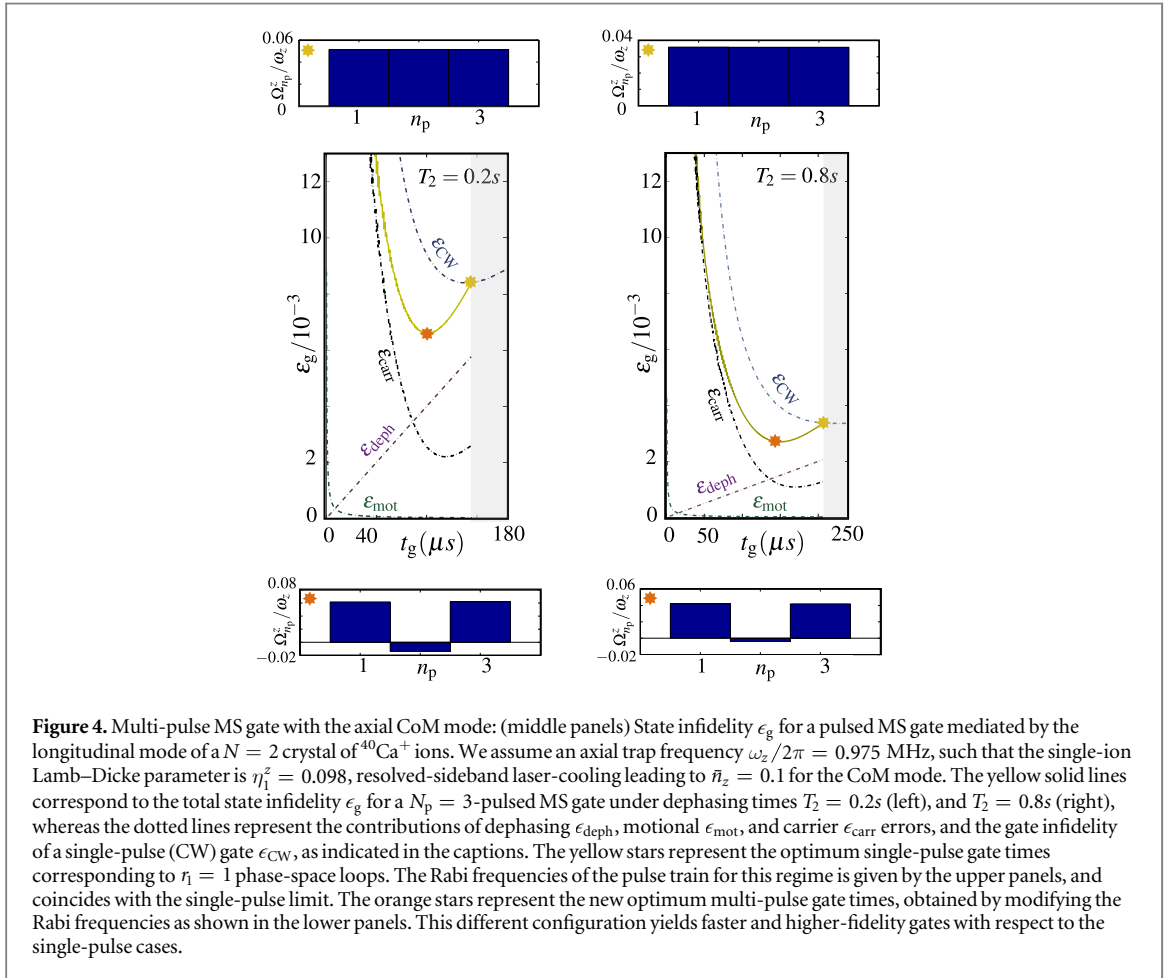


Figure 4. Multi-pulse MS gate with the axial CoM mode: (middle panels) State infidelity ϵ_g for a pulsed MS gate mediated by the longitudinal mode of a $N = 2$ crystal of $^{40}\text{Ca}^+$ ions. We assume an axial trap frequency $\omega_z/2\pi = 0.975$ MHz, such that the single-ion Lamb–Dicke parameter is $\eta_1^z = 0.098$, resolved-sideband laser-cooling leading to $\bar{n}_z = 0.1$ for the CoM mode. The yellow solid lines correspond to the total state infidelity ϵ_g for a $N_p = 3$ -pulsed MS gate under dephasing times $T_2 = 0.2s$ (left), and $T_2 = 0.8s$ (right), whereas the dotted lines represent the contributions of dephasing ϵ_{deph} , motional ϵ_{mot} , and carrier ϵ_{CW} errors, and the gate infidelity of a single-pulse (CW) gate ϵ_{CW} , as indicated in the captions. The yellow stars represent the optimum single-pulse gate times corresponding to $r_1 = 1$ phase-space loops. The Rabi frequencies of the pulse train for this regime is given by the upper panels, and coincides with the single-pulse limit. The orange stars represent the new optimum multi-pulse gate times, obtained by modifying the Rabi frequencies as shown in the lower panels. This different configuration yields faster and higher-fidelity gates with respect to the single-pulse cases.

the off-resonant carrier. This is the main difference with the more-demanding schemes [33–37] for arbitrary-speed gates that are not based on the resolved-sideband regime (57).

(b) *Addressing both vibrational modes.* We now study how to increase the gate speed of the single-pulse gates based on both transverse modes (see figure 3). In this case, the vibrational frequencies are closely spaced, and we need to close all phase-space trajectories using $N_p = 2N + 1$ pulses. We follow the above method to find the optimal pulse sequence for a fixed detuning and a certain gate time. Starting from the gate time of the highest-fidelity MS gates (see the stars in figure 3), we lower the target gate time, and search for pulse sequences that close all phase-space trajectories for a fixed detuning (99) that does no longer fulfill equation (103).

In figure 5, we represent the estimated infidelity of a $N_p = 5$ -pulse MS gate for $N = 2$ ions, as a function of the achieved gate time. In analogy to the axial MS gates in figure 4, we show that an additional speed-up can be obtained by a pulse train with state-dependent forces that alternate their direction (see lower panels). As every-other pulse becomes very weak, we can reduce the required average Rabi frequency with respect to the single-pulse gate, and thus obtain a higher fidelity. However, increasing the gate speed beyond an optimum point (orange stars) leads to an increase of the infidelity due to the contribution of the off-resonant carrier.

Although these results show that the error reduction by moving onto pulsed MS gates is not that large, the improvement in gate speed with respect to the optimal single-pulse gate can be substantial if one only wants to maintain the gate error to the same level. As discussed previously, increasing the speed even further in both of these pulsed schemes leads to an increase in the infidelity due to the off-resonant carrier. In the following section, we explore the advantage of exploiting the intrinsic micromotion to improve the gate speed even further, while simultaneously maintaining error rates below a given threshold.

3.3.2. Entangling gates with micromotion forces

After this long exposition, we have all the required ingredients to understand how the different MS gate schemes presented above can be improved by exploiting the ion-crystal intrinsic micromotion. Considering the regime (78), one can use directly the previous equations for the secular MS gates discussed in section 3.3.1, but taking into account the particular expressions for the micromotion off-resonant carrier (77) and the micromotion state-dependent forces (80). This simply amounts to substituting in all equations of section 3.3.1: the laser MS detunings by $\delta \rightarrow \tilde{\delta}$, the Rabi frequencies of the secular state-dependent forces by $\Omega_i^\alpha \rightarrow \tilde{\Omega}_i^\alpha = \Omega_i^\alpha q_\alpha/4$, and

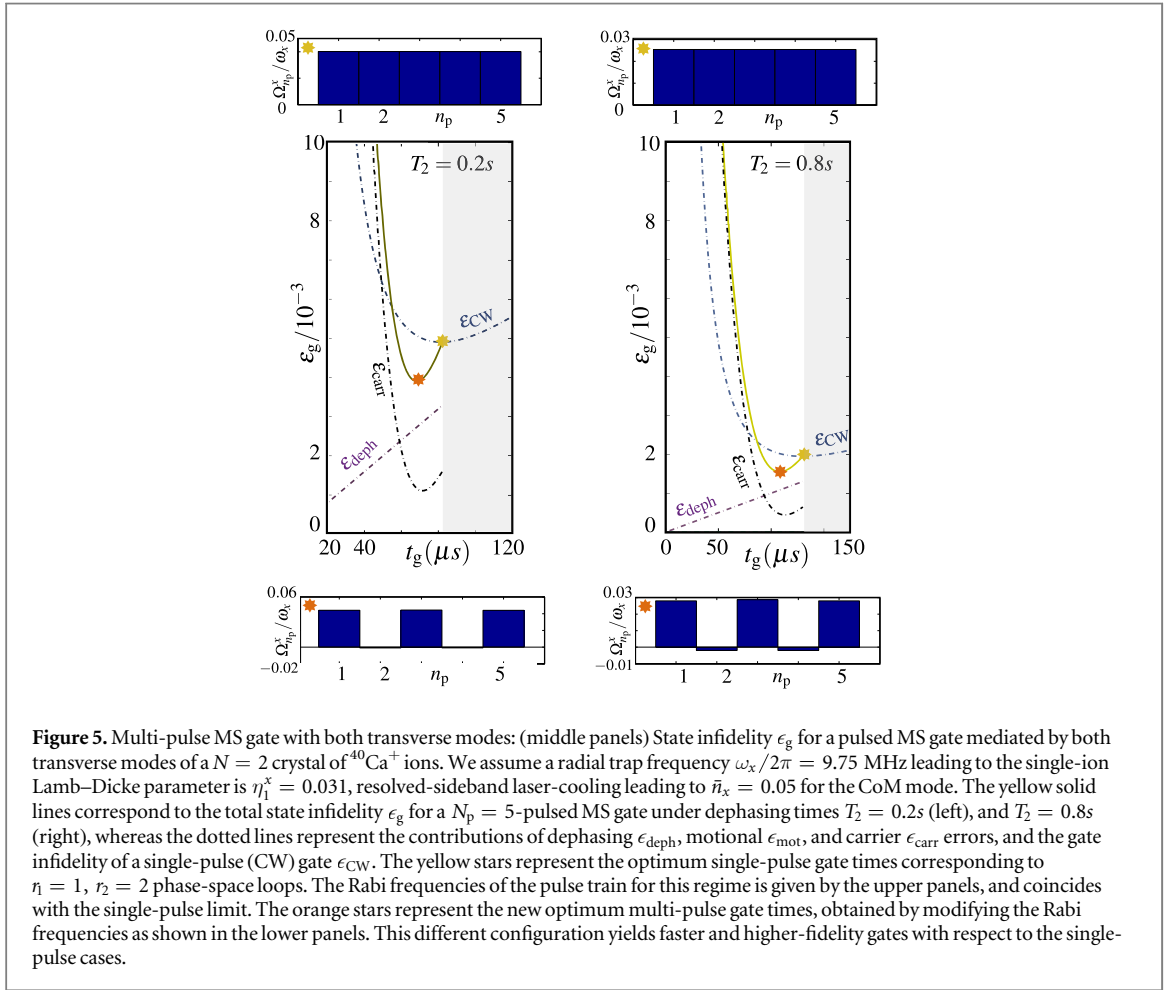


Figure 5. Multi-pulse MS gate with both transverse modes: (middle panels) State infidelity ϵ_g for a pulsed MS gate mediated by both transverse modes of a $N = 2$ crystal of $^{40}\text{Ca}^+$ ions. We assume a radial trap frequency $\omega_x/2\pi = 9.75$ MHz leading to the single-ion Lamb–Dicke parameter is $\eta_1^x = 0.031$, resolved-sideband laser-cooling leading to $\bar{n}_x = 0.05$ for the CoM mode. The yellow solid lines correspond to the total state infidelity ϵ_g for a $N_p = 5$ -pulsed MS gate under dephasing times $T_2 = 0.2s$ (left), and $T_2 = 0.8s$ (right), whereas the dotted lines represent the contributions of dephasing ϵ_{deph} , motional ϵ_{mot} , and carrier ϵ_{carr} errors, and the gate infidelity of a single-pulse (CW) gate ϵ_{CW} . The yellow stars represent the optimum single-pulse gate times corresponding to $n_1 = 1, n_2 = 2$ phase-space loops. The Rabi frequencies of the pulse train for this regime is given by the upper panels, and coincides with the single-pulse limit. The orange stars represent the new optimum multi-pulse gate times, obtained by modifying the Rabi frequencies as shown in the lower panels. This different configuration yields faster and higher-fidelity gates with respect to the single-pulse cases.

the error due to the off-resonant carrier by $\epsilon_{carr} \approx N \overline{(\Omega^\alpha)^2} / 2\delta^2 \rightarrow \tilde{\epsilon}_{carr} = 8N \overline{(\tilde{\Omega}^\alpha)^2} / q_\alpha^2 \Omega_{rf}^2$, where we have further assumed that micromotion compensation fulfills

$$\tilde{\beta}_i \ll \frac{q_\alpha \omega_\alpha}{4\Omega_{rf}}, \quad (107)$$

which is consistent with the experimentally achieved values that will be discussed in section 4.1. This equation gives a practical bound on how small the excess micromotion must be in order for our analysis to be correct.

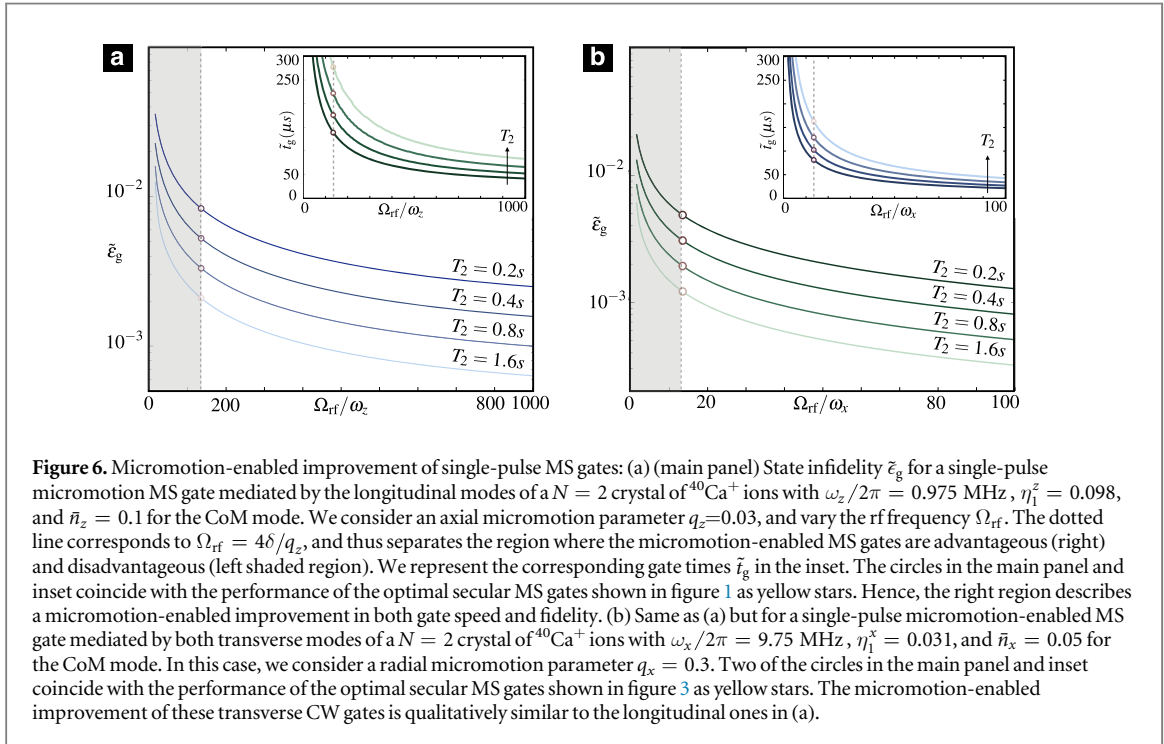
From these substitutions, one observes that the strength of the micromotion state-dependent dipole forces is reduced with respect to the one of the state-dependent secular forces (68) by a factor of $q_\alpha/4$. Therefore, more powerful lasers will be required to achieve the typical speed of secular MS gates in figures 1–5. However, provided that such laser sources are available, the maximum Rabi frequency will not be limited by $|\Omega_i^\alpha| \ll \delta$ as occurred for the secular MS scheme (72), but instead by $|\Omega_i^\alpha| \ll \Omega_{rf}$. Hence, exploiting the intrinsic micromotion, one can either maintain the gate speed while increasing the gate fidelity achieved by the secular MS schemes, or vice versa.

Qualitatively, for the same gate speed, the leading carrier error for micromotion-enabled MS gates $\tilde{\epsilon}_{carr}$ and secular MS gates ϵ_{carr} is related by $\tilde{\epsilon}_{carr} = \epsilon_{carr} (4\delta/q_\alpha \Omega_{rf})^2$. Hence, the carrier error will be reduced provided that

$$\delta < \frac{q_\alpha}{4} \Omega_{rf}, \quad (108)$$

where $\delta \sim \omega_\alpha$. As announced below equation (79), the advantage of the scheme will be larger, the smaller the ratio $\omega_\alpha/\Omega_{rf}$ can be made in the experiment. The microscopic trap parameter $q_\alpha/4$, which controls the relative amplitude of the intrinsic micromotion and the secular oscillations (14), sets how small is the ratio $\omega_\alpha/\Omega_{rf}$ required to be for the scheme to be advantageous. From a different perspective, this inequality shows that the coupling to the first micromotion sideband has to be sufficiently big for the scheme to become advantageous.

Conversely, if we want to increase the gate speed but maintain the fidelity of the secular MS gates, one can show that the gate times t_g of single-pulse secular schemes in equations (95) or equation (103) are related to the micromotion-enabled gate times \tilde{t}_g as follows $\tilde{t}_g = t_g (4\delta/q_\alpha \Omega_{rf})$. Accordingly, provided that the parameter regime (108) is achieved, there will be a speed-up of the entangling gates. A similar speed-up will also take place for the multi-pulsed MS gates.



To be more quantitative, we now study the total gate infidelity \tilde{z}_g for the micromotion-enabled version of the secular MS schemes of section 3.3.1. Therefore, in addition to the change in the carrier error already discussed, we also consider the dephasing and motional contributions to the gate infidelity. We extract the optimal gate time \tilde{t}_g that minimizes the gate infidelity \tilde{z}_g^{min} , and represent these two quantities as a function of the ratio $\Omega_{\text{rf}}/\omega_\alpha$, which determines the region where the micromotion scheme becomes advantageous (108).

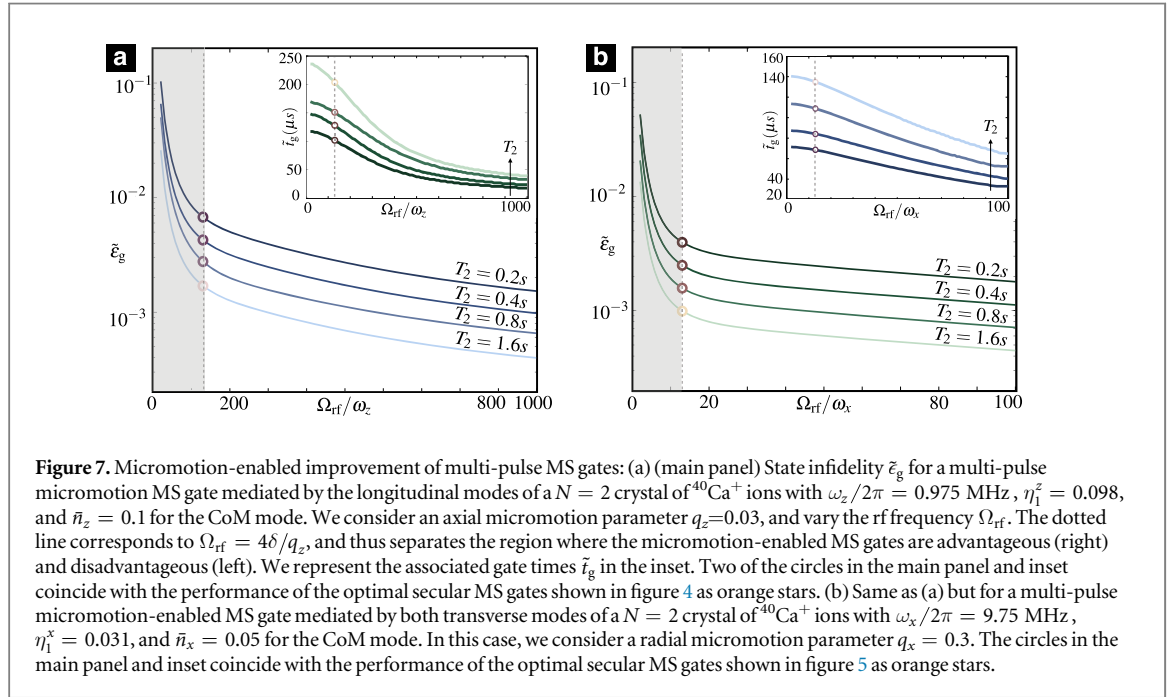
In figure 6, we study the micromotion version of the single-pulse secular MS gates mediated by longitudinal (figure 1) and transverse (figure 3) phonon modes. The circles correspond to rf frequencies that fulfill $\Omega_{\text{rf}} = 4\delta/q_\alpha$, such that the performance of the micromotion-enabled gates coincides with that of the standard secular MS gates. For larger rd frequencies (non-shaded regions), the micromotion scheme provides simultaneously lower gate errors (main panel) and lower gate times (inset), both for the MS gates mediated by longitudinal (figure 6 (a)) and transverse (figure 6 (b)) vibrational bus modes. A similar improvement is found in figure 7 for the micromotion version of the multi-pulse secular MS gates mediated by longitudinal (figure 4) and transverse (figure 5) phonon modes. Let us remark that this micromotion-enabled improvement of multi-pulse MS gates differs from the results presented in [42]. Here, Shen *et al* derive sequences for fast entangling gates to mitigate the adversarial effect of the excess micromotion of planar crystals. In our scheme, we exploit the intrinsic micromotion instead, and turn its effect into a feature that may allow one to improve on both fidelity and speed of phonon-mediated entangling quantum gates.

4. Experimental considerations

In this section, we discuss the experimental prospects of reaching the required parameter regime that would lead to the micromotion-enabled improvement of the entangling gates described above. We start by discussing in section 4.1 the state-of-the-art excess micromotion compensation, and the possibility of reaching the desired range in equation (107). In section 4.2, we discuss the difficulty of fulfilling equation (108) with current trap designs, and the prospects of satisfying it with realistic trap designs that may become accessible in the future.

4.1. Compensation of excess micromotion

Excess micromotion can give rise to a series of undesired effects [47], such as (i) a parametric heating that can increase the secular motion of ion crystals, limiting the temperatures achieved by laser cooling or even inducing crystal instabilities [61], (ii) a laser heating for parameters where laser cooling would be expected in the absence of excess micromotion [61], which can also be caused by the intrinsic micromotion [62], and (iii) motional shifts of frequency standards (e.g. second-order Doppler shifts) [47]. Therefore, a great deal of experimental effort has been devoted over the years to develop methods for a precise estimation and minimization of the excess micromotion. These methods range from (a) monitoring the change of the ion equilibrium position as the



secular trap frequencies are modified, to (b) comparing the fluorescence intensities of emitted photons when the lasers are tuned either to the bare carrier $\delta \approx 0$ or to the micromotion carrier $\delta \approx \Omega_{\text{rf}}$ (i.e. resolved-sideband regime), and (c) monitoring cross correlations of the time delay between the emitted photons and the rf signal (i.e. unresolved-sideband regime). The precision of method (a) is limited by the resolution limit of the optics that measures the ion position, whereas that of (b), (c) depends on limitations and noise on the laser and rf sources.

Provided that one of these methods yields an accurate measurement of excess micromotion, one can either apply additional electric fields to compensate the force of the spurious dc fields (5) due to patch potentials or unevenly coated electrodes, or load the electrodes with reactances to compensate the spurious asymmetries leading to the oscillating force of the ac fields in equation (5) (see the discussion in [47]). A detailed account of the achieved minimization of excess micromotion from different experimental groups can be found in [50], which shows that a careful compensation with different methods typically achieves β -parameters (64) on the order of $\beta_i \sim 10^{-3}$. Using tightly focused dipole beams to probe the ion position can be exploited to achieve even better micromotion compensation [63], so it is reasonable to consider that the β -parameter can attain values in the range $\beta_i \sim 10^{-4} - 10^{-3}$. We note that a realistic value for the ideal Paul trap parameters in equation (4) yields $q_\alpha \sim 0.2 - 0.3$ for the transverse directions $\alpha = \{x, y\}$, such that the desired compensation regime in equation (107) can be achieved with state-of-the-art trapped-ion technology. For the axial direction, considering short segmented linear traps, one may achieve ratios of $q_z/q_x \approx 10^{-3}$ [64]. Considering the performance of the axial micromotion-enabled entangling gates of figures 6(a) and 7(a) for $q_z = 0.03$, the smaller values of q_z for these segmented traps would require a much higher ratio of $\Omega_{\text{rf}}/\omega_z$, as well as a much higher laser power to achieve similar gate speeds. Accordingly, finding experimental trap designs that meet the requirements for a micromotion-enabled improvement based on axial modes seems very challenging, and this motivates us to consider the radial micromotion gates below.

4.2. Discussion of current and future trap designs

The suggested scheme requires a large ratio of the drive frequency to the secular motional frequency in the radial direction $\Omega_{\text{rf}}/\omega_x$. Since the confinement properties of ion traps can be accurately described by Mathieu equations that are independent on the actual trap geometry [65], a study based on a geometry that is suitable for usual trapping parameters will also suffice to explore the possibility of reaching the required parameters for a micromotion-enabled improvement of the entangling gate. Current traps for QIP operate usually in the regime of $\Omega_{\text{rf}}/\omega_x \approx 10 - 20$ [66, 67]. Experimentally, multi-qubit gate operations with $\Omega_{\text{rf}}/\omega_x = 46$ have already been demonstrated using $^{40}\text{Ca}^+$ [68, 69]. This ratio, together with the rest of the parameters used in figure 6(b), would already yield a benefit from the micromotion-enabled entangling gates. To be more precise, assuming a decoherence time of $T_2 = 0.8$ s and the error model described above, the single-pulse MS gate based on secular radial forces would reach $\epsilon_g = 2 \times 10^{-3}$ in a time $t_g = 129 \mu\text{s}$, whereas the one based on micromotion radial forces could attain $\epsilon_g = 8 \times 10^{-4}$ in a time $t_g = 57 \mu\text{s}$. Let us note that to gain full advantage of the protocol, one would need even higher ratios of $\Omega_{\text{rf}}/\omega_x$, which have not been achieved yet in experiments.

While there is no fundamental reason that will prohibit reaching even higher drive frequencies, one needs to take practical considerations into account. The dissipated power inside the trap will increase since the amplitude of the rf drive voltage needs to be increased, leading thus to a higher power dissipation in the trap itself, and also in the electrical connections to the trap [67]. Managing the increased heat load will require complex thermal management techniques, especially in the context of cryogenic systems. In this context, a smaller trap and connection capacitance is beneficial as it will facilitate the design of the required circuitry to generate the radio frequency trapping fields [67].

4.3. Technical noise sources

Estimating the error budget accounting for additional technical limitations can, for the proposed gate scheme, be performed analogously to other high-fidelity entangling gate operations, as detailed for instance in [31]. Regarding the differences for the micromotion-enabled gates, let us note that, in case that the experimentally available laser power is limited, the gate duration would be increased by a factor of $1/\sqrt{q_\alpha}$, which follows from the different scaling of the dipole forces in equations (73) and (80). In general, this would make the gate more susceptible to dephasing noise. Accordingly, if laser power is the limiting factor, one should consider continuous [24, 25] or pulsed [70] dynamical decoupling techniques to combat this noise.

Another technical aspect that would differ from entangling gates that do not make explicit use of micromotion is the generation of the bichromatic light fields. In the presented gate, the frequency of the beat note must be on the order of $2\Omega_{\text{rf}} \approx 2\pi \cdot 100$ MHz, whereas for the standard gate the modulation frequency is on the order of $\omega_\alpha/2\pi \approx 1\text{--}10$ MHz. The modulation is usually generated using acousto-optical modulators, which are available with a bandwidth of 100 MHz, at the cost of a reduced diffraction efficiency. This larger detuning from the carrier transition in our scheme brings the additional advantage that incoherent excitation of the qubit due to residual laser intensity at the carrier transition is reduced considerably. This incoherent excitation poses a major problem for qubits driven by narrow linewidth diode laser systems [71].

5. Conclusions and outlook

In this work, we have developed a set of theoretical tools to analyze the effects of excess and intrinsic micromotion in the schemes for high-fidelity quantum logic gates with trapped-ion qubits. We have shown that, in situations where the excess micromotion is compensated to a high degree, it is possible to exploit the intrinsic micromotion to improve on both the speed and fidelity of current schemes for entangling gates. We have derived a set of conditions that identify the parameter regime where such an improvement can occur, and discussed the possible challenges of reaching this regime considering realistic experimental conditions.

Aside from the particular gate scheme, we have presented for the first time a detailed quantum-mechanical treatment of intrinsic and excess micromotion in arbitrarily large chains of trapped ions. This has allowed us to develop a generic theory for the laser-ion interaction in the presence of micromotion, which might be useful for future trapped-ion studies in completely different contexts.

Acknowledgments

We thank J Home, J Alonso, and T Mehlstäubler for useful conversations, and H Landa and A Lemmer for their comments and the careful reading of the manuscript.

The research is based upon work supported by the Office of the Director of National Intelligence (ODNI), Intelligence Advanced Research Projects Activity (IARPA), via the US Army Research Office Grant No. W911NF-16-1-0070. The views and conclusions contained herein are those of the authors and should not be interpreted as necessarily representing the official policies or endorsements, either expressed or implied, of the ODNI, IARPA, or the US Government. The US Government is authorized to reproduce and distribute reprints for Governmental purposes notwithstanding any copyright annotation thereon. Any opinions, findings, and conclusions or recommendations expressed in this material are those of the author(s) and do not necessarily reflect the view of the US Army Research Office.

We also acknowledge support by US ARO through Grant No. W911NF-14-1-010. AB acknowledges support from Spanish MINECO Project FIS2015-70856-P, and CAM regional research consortium QUITEMAD+. PS, TM and RB acknowledge support from the Austrian Science Fund (FWF), through the SFB FoQus (FWF Project No. F4002-N16) and the Institut für Quanteninformation GmbH.

References

- [1] Nielsen M A and Chuang I L 2004 *Quantum Computation and Quantum Information* (Cambridge: Cambridge University Press)

- [2] Shor P W 1997 *SIAM J. Sci. Stat. Comput.* **26** 1484
- [3] Feynman R P 1982 *Int. J. Theor. Phys.* **21** 467
- [4] See Ladd T, Jelezko F, Laflamme R, Nakamura Y, Monroe C and O'Brien J L 2010 *Nature* **464** 45
- [5] See Wineland D J, Monroe C, Itano W M, Leibfried D, King B E and Meekhof D M 1998 *J. Res. Natl Inst. Stand. Technol.* **103** 259
- [6] See Leibfried D, Blatt R, Monroe C and Wineland D 2003 *Rev. Mod. Phys.* **75** 281
- [7] See Haeffner H, Roos C F and Blatt R 2008 *Phys. Rep.* **469** 155
- [8] Cirac J I and Zoller P 1995 *Phys. Rev. Lett.* **74** 4091
- [9] Schmidt-Kaler F, Häffner H, Riebe M, Gulde S, Lancaster G P T, Deuschle T, Becher C, Roos C F, Eschner J and Blatt R 2003 *Nature* **422** 408
- [10] Kielpinski D, Monroe C and Wineland D J 2002 *Nature* **417** 709
- [11] Landauer R 1995 *Phil. Trans. R. Soc. A* **3** 367
Landauer R 1996 *Phys. Lett. A* **217** 188
- [12] Unruh W G 1995 *Phys. Rev. A* **51** 992
- [13] Shor P W 1995 *Phys. Rev. A* **52** 2493(R)
Calderbank A R and Shor P W 1996 *Phys. Rev. A* **54** 1098
Steane A M 1996 *Phys. Rev. Lett.* **77** 793
- [14] Kitaev A Y 2003 *Ann. Phys.* **303** 2
Bombin H and Martin-Delgado M A 2006 *Phys. Rev. Lett.* **97** 180501
- [15] Knill E 2010 *Nature* **463** 441
- [16] Chiaverini J et al 2004 *Nature* **432** 602
- [17] Nigg D, Müller M, Martinez E A, Schindler P, Hennrich M, Monz T, Martin-Delgado M A and Blatt R 2014 *Science* **345** 302
- [18] Linke N M, Gutierrez M, Landsman K A, Figgatt C, Debnath S, Brown K R and Monroe C 2016 arXiv:1611.06946
- [19] Lidar D A, Chuang I L and Whaley K B 1998 *Phys. Rev. Lett.* **81** 2594
- [20] Kielpinski D, Meyer V, Rowe M A, Sackett C A, Itano W M, Monroe C and Wineland D J 2001 *Science* **291** 1013
Monz T et al 2009 *Phys. Rev. Lett.* **103** 200503
- [21] Bollinger J J, Heizen D J, Itano W M, Gilbert S L and Wineland D J 1991 *IEEE Trans. Instrum. Meas.* **40** 126
Langer C et al 2005 *Phys. Rev. Lett.* **95** 060502
- [22] Viola L, Knill E and Lloyd S 1999 *Phys. Rev. Lett.* **82** 2417
Viola L, Lloyd S and Knill E 1999 *Phys. Rev. Lett.* **83** 4888
- [23] Biercuk M, Uys H, VanDevender A P, Shiga N, Itano W M and Bollinger J J 2009 *Nature* **458** 996
- [24] Bermudez A, Schmidt P O, Plenio M B and Retzker A 2012 *Phys. Rev. A* **85** 040302(R)
Lemmer A, Bermudez A and Plenio M B 2013 *New J. Phys.* **15** 083001
- [25] Tan T R, Gaebler J P, Bowler R, Lin Y, Jost J D, Leibfried D and Wineland D J 2013 *Phys. Rev. Lett.* **110** 263002
Wilson A C, Colombe Y, Brown K R, Knill E, Leibfried D and Wineland D J 2014 *Nature* **512** 57
- [26] Milburn G J, Schneider S and James D F V 2000 *Fortschr. Phys.* **48** 801
- [27] Leibfried D et al 2003 *Nature* **422** 412
- [28] Sørensen A and Mølmer K 1999 *Phys. Rev. Lett.* **82** 1971
Sørensen A and Mølmer K 2000 *Phys. Rev. A* **62** 022311
- [29] Sackett C A et al 2000 *Nature* **404** 256
- [30] Benhelm J, Kirchmair G, Roos C F and Blatt R 2008 *Nat. Phys.* **4** 463
- [31] Ballance C J, Harty T P, Linke N M, Sepiol M A and Lucas D M 2016 *Phys. Rev. Lett.* **117** 060504
- [32] Gaebler J P et al 2016 *Phys. Rev. Lett.* **117** 060505
- [33] García-Ripoll J J, Zoller P and Cirac J I 2003 *Phys. Rev. Lett.* **91** 157901
García-Ripoll J J, Zoller P and Cirac J I 2005 *Phys. Rev. A* **71** 062309
Duan L M 2004 *Phys. Rev. Lett.* **93** 100502
- [34] Bentley C D B, Carvalho A R R and Hope J J 2015 *New J. Phys.* **17** 103025
- [35] Bentley C D B, Taylor R L, Carvalho A R R and Hope J J 2016 *Phys. Rev. A* **93** 042342
- [36] See Mizrahi J, Neyenhuis B, Johnson K G, Campbell W C, Senko C, Hayes D and Monroe C 2014 *Appl. Phys. B* **114** 45
- [37] Cohen I, Rotem A and Retzker A 2016 *Phys. Rev. A* **93** 032340
- [38] Steane A M, Imreh G, Home J P and Leibfried D 2014 *New J. Phys.* **16** 053049
- [39] Lee P J, Brickman K-A, Deslauriers L, Haljan P C, Duan L-M and Monroe C 2005 *J. Opt. B: Quantum Semiclass. Opt.* **7** S371
- [40] Roos C F 2008 *New J. Phys.* **10** 013002
- [41] Turchette Q A, Wood C S, King B E, Myatt C J, Leibfried D, Itano W M, Monroe C and Wineland D J 1998 *Phys. Rev. Lett.* **81** 3631
- [42] Shen C and Duan L-M 2014 *Phys. Rev. A* **90** 022332
- [43] Wang S-T, Shen C and Duan L-M 2015 *Sci. Rep.* **5** 8555
- [44] Landa H, Retzker A, Schaetz T and Reznik B 2014 *Phys. Rev. Lett.* **113** 053001
- [45] Blakestad R B, Ospelkaus C, VanDevender A P, Wesenberg J H, Biercuk M J, Leibfried D and Wineland D J 2011 *Phys. Rev. A* **84** 032314
- [46] Chiaverini J, Blakestad B R, Britton J W, Jost J D, Langer C, Leibfried D G, Ozeri R and Wineland D J 2005 *Quantum Inf. Comput.* **5** 419
- [47] Berkeland D J, Miller J D, Bergquist J C, Itano W M and Wineland D J 1998 *J. Appl. Phys.* **83** 5025
- [48] Abramowitz M and Stegun I A 1972 *Handbook of Mathematical Functions with Formulas, Graphs, and Mathematical Tables* (New York: Dover)
- [49] Boyce W E and DiPrima R C 2001 *Elementary Differential Equations and Boundary Value Problems* (New York: Wiley)
- [50] Keller J, Partner H L, Burgermeister T and Mehlstäubler T E 2015 *J. Appl. Phys.* **118** 104501
Keller J, Burgermeister T, Kalincev D, Kiethe J and Mehlstäubler T E 2015 arXiv:1512.05677
- [51] Glauber R J 1992 *Quantum Theory of Particle Trapping by Oscillating Fields*, in *Quantum Measurements in Optics* ed P Tomba and D F Walls (New York: Plenum)
- [52] Feynman R P 1982 *Statistical Mechanics: A Set of Lectures* (Reading: Benjamin-Cummings)
- [53] James D F V 1998 *Appl. Phys. B* **66** 181
- [54] Landa H, Drewsen M, Reznik B and Retzker A 2012 *New J. Phys.* **14** 093023
- [55] Kaufmann H, Ulm S, Jacob G, Poschinger U, Landa H, Retzker A, Plenio M B and Schmidt-Kaler F 2012 *Phys. Rev. Lett.* **109** 263003
- [56] Watson G N 1995 *A Treatise on the Theory of Bessel Functions* (Cambridge: Cambridge University Press)
- [57] Magnus W 1954 *Commun. Pure Appl. Math.* **7** 649
Blanes S, Casas F, Oteo J A and Ros J 2010 *Eur. J. Phys.* **31** 907

- [58] Schindler P et al 2013 *New J. Phys.* **15** 123012
- [59] Zhu S-L, Monroe C and Duan L-M 2006 *Europhys. Lett.* **73** 485
Zhu S-L, Monroe C and Duan L-M 2006 *Phys. Rev. Lett.* **97** 050505
- [60] Choi T, Debnath S, Manning T A, Figgatt C, Gong Z-X, Duan L-M and Monroe C 2014 *Phys. Rev. Lett.* **112** 190502
- [61] DeVoe R G, Hoffnagle J and Brewer R G 1989 *Phys. Rev. A* **39** 4362
- [62] Cirac J I, Garay L J, Blatt R, Parkins A S and Zoller P 1994 *Phys. Rev. A* **49** 421
- [63] Huber T, Lambrecht A, Schmidt J, Karpa L and Schaetz T 2014 *Nat. Commun.* **5** 5587
- [64] Herschbach N, Pyka K, Keller J and Mehlstäubler T E 2012 *App. Phys. B* **107** 891
- [65] Major F G, Gheorghe V N and Werth G 2005 *Charged Particle Traps* (Berlin: Springer)
- [66] Brandl M F et al 2016 *Rev. Sci. Instrum.* **87** 113103
- [67] Brandl M F, Schindler P, Monz T and Blatt R 2016 *Appl. Phys. B* **122** 157
- [68] Alonso J 2017 private communication
- [69] de Clercq L E, Lo H, Marinelli M, Nadlinger D, Oswald R, Negnevitsky V, Kienzler D, Keitch B and Home J P 2016 *Phys. Rev. Lett.* **116** 080502
- [70] Manovitz T, Rotem A, Shaniv R, Cohen I, Shapira Y, Akerman N, Retzker A and Ozeri R 2017 arXiv:1706.03468
- [71] Akerman N, Navon N, Kotler S, Glickman Y and Ozeri R 2015 *New J. Phys.* **17** 113060
- [72] Aharonov D and Ben-Or M 1997 *Proc. 29th Annual ACM Symp. on Theory of Computing* p 176
- [73] Blümel R, Kappler C, Quint W and Walther H 1989 *Phys. Rev. A* **40** 808